Journal of *Marine Science and Engineering*

MDPI

Article

Mathematical Modeling of Two-Dimensional Depth Integrated Nonlinear Coupled Boussinesq-Type Equations for Shallow-Water Waves with Ship-Born Generation Waves in Coastal Regions

Vinita and Prashant Kumar *

Department of Applied Sciences, National Institute of Technology, Delhi 110036, India; vinita@nitdelhi.ac.in
* Correspondence: prashantkumar@nitdelhi.ac.in

Abstract: A hybrid computational framework integrating the finite volume method (FVM) and finite difference method (FDM) is developed to solve two-dimensional, time-dependent nonlinear coupled Boussinesq-type equations (NCBTEs) based on Nwogu's depth-integrated formulation. This approach models nonlinear dispersive wave forces acting on a stationary vessel and incorporates a frequency dispersion term to represent ship-wave generation due to a localized moving pressure disturbance. The computational domain is divided into two distinct regions: an inner domain surrounding the ship and an outer domain representing wave propagation. The inner domain is governed by the three-dimensional Laplace equation, accounting for the region beneath the ship and the confined space between the ship's right side and a vertical quay wall. Conversely, the outer domain follows Nwogu's 2D depth-integrated NCBTEs to describe water wave dynamics. Interface conditions are applied to ensure continuity by enforcing the conservation of volume flux and surface elevation matching between the two regions. The accuracy of this coupled numerical scheme is verified through convergence analysis, and its validity is established by comparing the simulation results with prior studies. Numerical experiments demonstrate the model's capability to capture wave responses to simplified pressure disturbances and simulate wave propagation over intricate bathymetry. This computational framework offers an efficient and robust tool for analyzing nonlinear wave interactions with stationary ships or harbor structures. The methodology is specifically applied to examine the response of moored vessels to incident waves within Paradip Port, Odisha, India.

Keywords: nonlinear coupled Nwogu's Boussinesq-type equation; coupled hybrid finite volume finite difference method; solitary waves; regular waves; water wave propagation

check for updates

Academic Editors: Guang Yin and Muk Chen Ong

Received: 9 February 2025
Revised: 26 February 2025
Accepted: 11 March 2025
Published: 13 March 2025

Citation: Vinita; Kumar, P. Mathematical Modeling of Two-Dimensional Depth Integrated Nonlinear Coupled Boussinesq-Type Equations for Shallow-Water Waves with Ship-Born Generation Waves in Coastal Regions. *J. Mar. Sci. Eng.* **2025**, *13*, 562. https://doi.org/10.3390/jmse13030562

Copyright: © 2025 by the authors. Licensee MDPI, Basel, Switzerland. This article is an open access article distributed under the terms and conditions of the Creative Commons Attribution (CC BY) license (https://creativecommons.org/licenses/by/4.0/).

1. Introduction

Since the late 19th century, scientists and engineers have been interested in mathematical descriptions of vessel waves. Lord Kelvin first studied moving disturbances in deep water, creating an angle called the Kelvin wedge. This angle, which is a function of the dimensionless depth Froude number, was first described mathematically by Havelock [1]. The relationships between sailing speed and wave heights were initially documented by Franzius and Straub, and extensive laboratory study was conducted by Johnson [2].

Ports situated in coastal areas often encounter severe wave oscillations caused by high-energy incident waves from the open sea. These oscillations are particularly significant during extreme weather conditions, such as strong seasonal winds or typhoons, which

generate waves with amplitudes reaching several meters. For example, seasonal winds linked to typhoons in the Bay of Bengal have caused high wave heights of 3 to 5 m at the Paradip industrial port in Odisha, India. Extreme wave conditions like this present significant obstacles to port infrastructure and operations, particularly with regard to moored ships. These situations make the loading and unloading of cargo a complex task for port authorities. Although seasonal weather patterns cannot be controlled, precise mathematical models can be employed to analyze the motion of moored ships under resonant conditions.

Compared to 2D numerical approaches, 3D numerical models have been developed to account for additional factors such as bottom topography, which plays a crucial role in port resonance. This study is structured into two main aspects: harbor oscillations and the motion of moored ships. Earlier research has extensively focused on experimental and theoretical studies of harbor oscillations, particularly in simplified harbor geometries like circular and rectangular shapes [3,4]. Furthermore, the Helmholtz equation for constant-depth scenarios [5] and the Laplace equation for variable depth [6,7] have been solved using both 2D [8], and 3D boundary element methods (BEMs) [9,10]. Other phenomena influencing harbor resonance, such as irregular waves [7], long-period waves [11,12], and corner effects [6], have also been investigated.

Advanced models, including nonlinear Boussinesq equations, have been employed to study transient harbor oscillations induced by events like N-waves [13], solitary waves [14], and wave breaking [15]. Investigations into low-frequency wave resonance [16] have also been performed. The applications of these studies to real-world harbors, such as Pohang New Harbor in South Korea [11,17,18], Paradip Port in India, Marina di Carrara in Italy [19], Ferrol in Spain [20], and Long Beach Harbor in the United States [21], provide valuable insights into harbor dynamics. Harbor resonance and the motion of moored ships are critical aspects of coastal and maritime engineering. The interaction of incoming waves with complex harbor geometries can lead to significant oscillations, affecting port operations and vessel stability. Previous studies have extensively investigated methods to mitigate harbor resonance, including the effects of Bragg reflection and undulating topography on wave propagation and resonance suppression.

Bragg reflection, a phenomenon where periodic seabed topography scatters incoming waves, has been studied as a potential mechanism to control harbor oscillations. Notably, Ref. [22] analyzed the influence of Bragg reflection on harbor resonance triggered by irregular wave groups, highlighting the role of periodic topographic features in altering wave energy distribution. Furthermore, Ref. [23] explored the effects of Bragg reflection on harbor oscillations, demonstrating how wave interference patterns can modify resonance frequencies and amplitudes. These findings provide critical insights into the fundamental mechanisms of wave interaction with structured seabed configurations.

Additionally, Ref. [24] carried out a mechanism analysis on how periodic undulating topography mitigates harbor resonance. Their study provided quantitative assessments of how seabed modifications can effectively reduce wave-induced oscillations within enclosed harbor basins. The implementation of such techniques can lead to significant improvements in harbor tranquility and the stability of moored ships, particularly under varying depth conditions.

Given these advancements, it is crucial to integrate these findings into numerical models for predicting and mitigating harbor resonance effects. The present study extends this research by employing a hybrid finite volume and finite difference method to solve Nwogu's depth-integrated nonlinear coupled Boussinesq-type equations. This approach captures nonlinear dispersive wave forces acting on a fixed ship, thereby offering a robust framework for analyzing ship motion in complex harbor environments.

The study of moored ship motion under harbor resonance has garnered significant attention due to its practical implications in maritime engineering and port management. Various numerical methods have been employed to simulate such complex hydrodynamic phenomena. Among the most frequently utilized approaches are the boundary element method (BEM) [25,26], finite volume method (FVM) [27], finite difference method (FDM) [28], and boundary integral equation method (BIEM). These methodologies are essential for understanding wave-structure interactions and their consequences on moored vessels.

Recent advancements in computational mechanics have led to the development of hybrid numerical techniques, which integrate different methods to improve simulation accuracy and efficiency. For instance, the finite element method (FEM) [29–31] has been extensively adopted in fluid–structure interaction studies. The boundary element spectral method (BSEM) [32] has also emerged as a viable alternative for capturing complex wave behavior. Notably, BEMs and FEMs are combined in the hybrid finite element method (HFEM) [10] to analyze the dynamics of moored ships in harbors with varying depths and geometries.

The application of 3D Green's functions has further enhanced the predictive capabilities of numerical models, particularly in the analysis of ship motion in harbors with constant bathymetry [33–35]. Additionally, hybrid BEM–FEM models have been instrumental in simulating the motion of moored ships [36,37]. A seminal contribution by Yoo [38] introduced semi-circular artificial boundaries to comprehensively address the six fundamental modes of moored ship motion: surge, sway, heave, roll, pitch, and yaw. Furthermore, hybrid Boussinesq panel methods [39,40] and hybrid potential theories [41] have been developed to evaluate the influence of external wave forces, including tsunami-induced disturbances.

Studies on time-domain simulations have analyzed coupled interactions between floating vessels and mooring systems [42]. These studies have provided valuable insights into the dynamics of moored ships at various ports worldwide, such as the Port of Brisbane in Australia [43], the Port of A Coruña in Spain [44], and the Port of Santos in Brazil [45]. Understanding the impact of resonance conditions on moored ships at different ports is crucial for optimizing mooring configurations and mitigating potential risks [46–50].

This study integrates numerical simulations and experimental analyses to investigate the resonance phenomenon affecting fluid motions within the confined space between a moored ship, the seabed, and a vertical quay wall. We create a strong mathematical framework that takes into account the impacts of wave amplification by determining the natural frequency of fluid oscillations within the gap. The Boussinesq equations, supplemented by Newton's Second Law, form the foundation of our computational model. A novel algorithm is introduced to efficiently simulate nonlinear wave effects on ship sections adjacent to quay walls in harbor environments. The primary focus of this research is the characterization of the six modes of moored ship motion under resonant conditions at Paradip Port. A detailed parametric analysis is conducted to evaluate the role of draft-depth ratios in influencing ship dynamics. Numerical models are often used to identify safety zones for moored ships under resonance circumstances.

The structure of this document is as follows: The mathematical formulation of moored ship motion taking bathymetric fluctuations into account and the hybrid finite volume technique (FVM) and the finite difference method (FDM) used to solve the two-dimensional nonlinear coupled Boussinesq-type equations (NCBTEs) are described in Section 2. Section 3 provides a comprehensive validation of the numerical model through convergence analysis with numerical simulation results of the model. Section 4 presents the discussion and conclusion of the paper, focusing on wave impacts at key locations in Paradip Port, and also presents potential future research directions.

2. Material and Method

2.1. Model Formulation

At Jagatsingpur, Odisha, on India's east coast, where the Mahanadi River and the Bay of Bengal converge, the current numerical plan is put into practice at the actual Paradip Port. Consider the Cartesian coordinate system on the mean free surface, the y-axis points in the opposite direction of gravity and the x-axis points in the direction of incoming wave propagation. The practical simulation of ocean wave movements from deep to shallow water is made possible by Nwogu's (1993) enhancement of the dispersion properties of the traditional Boussinesq-type equations. These improvements enable the accurate modeling of wave refraction, diffraction, and nonlinear interactions, particularly in coastal environments. The hydraulic processes that are sub- and super-crucial define the surf-zone flow using the governing equations that are integrated with depth. This following section involves reformulating the widely utilized Boussinesq-type technique with conserved variables. The governing equations that arise are then rearranged in the conservative form of the nonlinear shallow-water equations for shock capturing. The reference water depth is given by $z_b = -0.531h(x,y)$. The total water depth $H(x,y,t) = h(x,y) + \eta(x,y,t)$, $h(x,y,t)$ is the variable water depth. The arbitrary domain is divided into several parts. The first part is the bounded region and the second part is the unbounded region, which is shown in Figure 1.

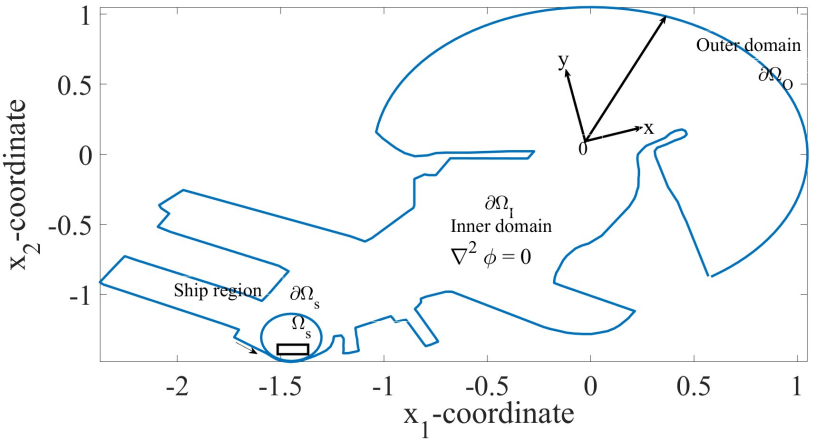


Figure 1. Layout of Paradip Port with moored ship.

Here, ϕ defines the velocity potential function in the x, y, z directions. The water wave propagation in the inner port domain with the ship region is described by the Laplace equation, while NCBTEs are utilized in the outer region domain, which includes variable topography. By rearranging the governing equations into their conservative form, they become analogous to the nonlinear shallow-water equations, thereby facilitating the application of shock-capturing schemes. This transformation ensures better numerical stability and accuracy when simulating wave breaking and other highly nonlinear phenomena.

2.2. Governing Equations for Outer Domain

The fluid is considered to be incompressible and inviscid, and the flow is irrotational. $\nabla \times \boldsymbol{u_\alpha} = 0$. The velocity components along the x- and y-directions are represented as $\boldsymbol{u_\alpha} = (u, v)$. The governing equations of Nwogu's depth integrated nonlinear coupled Boussinesq-type Equations (NCBTEs) are written as:

$$\frac{\partial \eta}{\partial t} + \nabla \cdot [(h+\eta)\boldsymbol{u_\alpha}] + \nabla \cdot \left\{ \left(\frac{z_\alpha^2}{2} - \frac{h^2}{6} \right) h\nabla(h \cdot \boldsymbol{u_\alpha}) + \left(z_\alpha + \frac{h}{2} \right) h\nabla(\nabla \cdot (h\boldsymbol{u_\alpha})) \right\} = 0 \quad (1)$$

and

$$\frac{\partial \boldsymbol{u_\alpha}}{\partial t} + g\nabla \cdot \eta + (\boldsymbol{u_\alpha} \cdot \nabla)u_\alpha + \frac{\partial}{\partial t}\left\{ \frac{z_\alpha^2}{2}\nabla(\nabla \cdot \boldsymbol{u_\alpha}) + z_\alpha \nabla(\nabla \cdot (h\boldsymbol{u_\alpha})) \right\} = -\frac{1}{\rho}\nabla \bar{P}, \tag{2}$$

where $\eta(x, y, t)$ describes the free surface elevation. The variable ρ denotes the fluid density, while $\bar{P}$ represents the pressure exerted at the water interface layer. The pressure expression is given by:

$$\bar{P} = D\frac{\partial^4 \eta}{\partial x^4} + Q\frac{\partial^2 \eta}{\partial x^2} + M\frac{\partial^2 \eta}{\partial t^2} \tag{3}$$

where the coefficients are defined as follows:

$$D = \frac{Ed^3}{12(1-\nu^2)}, \quad M = \rho d \tag{4}$$

Here, ν denotes Poisson's ratio, E represents the Young's modulus associated with water waves, and Q corresponds to the lateral stress in the plate, with $Q > 0$ indicating compression. The horizontal gradient operator is defined as:

$$\nabla = \left(\frac{\partial}{\partial x}, \frac{\partial}{\partial y}\right) \tag{5}$$

To proceed further, consider the following Nwogu's 2D depth integrated NCBTEs: Equations (1) and (2) are given as

$$\begin{aligned} &\frac{\partial \eta}{\partial t} + \frac{\partial}{\partial x}\Big[(h+\eta)u\Big] + \frac{\partial}{\partial y}[(h+\eta)v]_y + \frac{\partial}{\partial x}\Big[(\frac{z_b^2}{2} - \frac{h^2}{6})h\big(u_{xx} + v_{xy}\big) + \Big(z_b + \frac{h}{2}\Big) \\ &h\big((hu)_{xx} + (hv)_{xy}\big)\Big] + \frac{\partial}{\partial y}\Big[(\frac{z_b^2}{2} - \frac{h^2}{6})h\big(v_{yy} + u_{xy}\big) + \Big(z_b + \frac{h}{2}\Big)h\big((hv)_{yy} + (hu)_{xy}\big)\Big] = 0, \end{aligned} \tag{6}$$

$$\frac{\partial u}{\partial t} + u\frac{\partial u}{\partial x} + v\frac{\partial u}{\partial y} + g\frac{\partial \eta}{\partial x} + \frac{z_b^2}{2}\big(u_{xxt} + u_{xyt}\big) + z_b\big((hu_t)_{xx} + (hu_t)_{xy}\big) + \frac{1}{\rho}\frac{\partial \bar{P}}{\partial x} = 0, \tag{7}$$

$$\frac{\partial v}{\partial t} + v\frac{\partial v}{\partial y} + u\frac{\partial v}{\partial x} + g\frac{\partial \eta}{\partial y} + \frac{z_b^2}{2}\big(v_{yyt} + u_{xyt}\big) + z_b\big((hv_t)_{yy} + (hu_t)_{xy}\big) + \frac{1}{\rho}\frac{\partial \bar{P}}{\partial y} = 0. \tag{8}$$

Equations (6)–(8) can be rewritten by letting $\eta_t = (H-h)_t = \partial H/\partial t$; with $\partial h/\partial t = 0$, we have:

$$\frac{\partial H}{\partial t} + \frac{\partial}{\partial x}[(Hu)] + \frac{\partial}{\partial y}[(Hv)] + \Psi_c + \Psi_{mn} = 0. \tag{9}$$

The dispersion term in the continuity equation, denoted as Ψ_c, plays a crucial role in capturing higher-order effects in wave propagation models. Its formulation is given by:

$$\begin{aligned} \Psi_c = &\left[\left(\frac{z_b^2}{2} - \frac{h^2}{6}\right)h\big(u_x + v_y\big)_x + \left(z_b + \frac{h}{2}\right)h\big((hu)_x + (hv)_y\big)_x\right]_x \\ &+ \left[\left(\frac{z_b^2}{2} - \frac{h^2}{6}\right)h\big(u_x + v_y\big)_y + \left(z_b + \frac{h}{2}\right)h\big((hu)_x + (hv)_y\big)_y\right]_y. \end{aligned} \tag{10}$$

This term accounts for the dispersive characteristics of the wave field by incorporating depth-dependent contributions to the continuity equation. The mass source term, Ψ_{mn}, is introduced to facilitate spectral wave generation, ensuring consistency with energy conservation principles. Furthermore, in order to preserve stability and accuracy, extra considerations are needed for the momentum Equations (7) and (8), which describe fluid motion under the impact of external forces. These higher-order components improve the

model's capacity to forecast intricate wave dynamics, especially in applications related to coastal engineering where wave transformation, refraction, and diffraction are important factors. After the multiplication of these equations with total water depth, H, and using the relation $gH\nabla\eta = gH\nabla(H-\eta) = gh\nabla H - gH\nabla\, h = (gH^2/2)_x + gH\nabla z_b$, we get:

$$H\frac{\partial u}{\partial t} + Hu\frac{\partial u}{\partial x} + Hv\frac{\partial u}{\partial y} + gH\frac{\partial \eta}{\partial x} + H\frac{z_b^2}{2}\left(u_{xxt} + u_{xyt}\right) + Hz_b\left((hu_t)_{xx} + (hu_t)_{xy}\right) + H\frac{1}{\rho}\frac{\partial \bar{P}}{\partial x} = 0,$$

or we can write this in more compact form as:

$$\begin{aligned}&(Hu)_t + \left(H\left[\frac{z_b^2}{2}\left(u_{xx} + v_{xy}\right) + z_b\left((hu)_{xx} + (hv)_{xy}\right)\right]\right)_t + \frac{\partial}{\partial x}\left(Hu^2 + \frac{1}{2}gH^2\right)\\ &+ Hv\frac{\partial u}{\partial y} = -gH\frac{\partial z_b}{\partial x} - u\Psi_c + \Psi_{mx} - H\frac{1}{\rho}\frac{\partial \bar{P}}{\partial x}.\end{aligned} \tag{11}$$

Similarly, the other momentum equation for v takes the form:

$$\begin{aligned}&(Hv)_t + \left(H\left[\frac{z_b^2}{2}\left(v_{yyt} + v_{xyt}\right) + z_b\left((hv)_{yy} + (hu)_{xy}\right)\right]\right)_t + \frac{\partial}{\partial y}\left(Hv^2 + \frac{1}{2}gH^2\right)\\ &+ Hv\frac{\partial u}{\partial x} = -gH\frac{\partial z_b}{\partial y} - u\Psi_c + \Psi_{my} - H\frac{1}{\rho}\frac{\partial \bar{P}}{\partial y},\end{aligned} \tag{12}$$

The dispersion terms introduce complexity into the time integration of momentum equations. These terms are represented as:

$$\begin{aligned}\Psi_{mx} &= H\left\{\frac{z_b^2}{2}\left[u_{xx} + v_{xy}\right] + z_b\left[(hu)_{xx} + (hv)_{xy}\right]\right\}_t,\\ \Psi_{my} &= H\left\{\frac{z_b^2}{2}\left[u_{xyt} + v_{xyt}\right] + z_b\left[(hu)_{yy} + (hv)_{xy}\right]\right\}_t.\end{aligned} \tag{13}$$

Unlike the hydrostatic local acceleration terms, such as $(Hu)_t$ and $(Hv)_t$, in the nonlinear shallow-water equations (NSWEs), where momentum evolves over time, the temporal derivative only acts on the velocity components of these additional dispersive terms. To ensure consistency in incorporating momentum, the non-hydrostatic contribution in Equation (13) is reorganized using a straightforward product rule expansion:

$$\begin{aligned}H\left\{\frac{z_b^2}{2}\left[u_{xx} + v_{xy}\right] + z_b\left[(hu)_{xx} + (hv)_{xy}\right]\right\}_t &= H\left\{\frac{z_b^2}{2}\left[u_{xt} + v_{xy}\right]\right\}_t + Hz_b\left\{(hu)_{xx} + (hv)_{xy}\right\}_t\\ &- H_t\left\{\frac{z_\alpha^2}{2}\left[u_{xt} + v_{xy}\right] + z_b\left[(hu)_{xx} + (hv)_{xy}\right]\right\}.\end{aligned} \tag{14}$$

Similarly:

$$\begin{aligned}H\left\{\frac{z_b^2}{2}\left[u_{xy} + v_{yt}\right] + z_\alpha\left[(hu)_{xy} + (hv)_{yy}\right]\right\}_t &= H\left\{\frac{z_\alpha^2}{2}\left[u_{xy} + v_{yt}\right]\right\}_t + Hz_b\left\{(hu)_{xy} + (hv)_{yy}\right\}_t\\ &- H_t\left\{\frac{z_b^2}{2}\left[u_{xy} + v_{yt}\right] + z_\alpha\left[(hu)_{xy} + (hv)_{yy}\right]\right\}.\end{aligned} \tag{15}$$

Since the continuity equation is explicit, H_t can be obtained straight from the flow and dispersion terms in Equation (9) as follows:

$$-H_t = (Hu)_x + (Hv)_y + \Psi_c. \tag{16}$$

In Equations (14) and (15), terms with second-order derivatives, x or yy, can be separated and grouped with local acceleration terms as evolution variables P_1 and P_2:

$$P_1 = (Hu)_t + \left[0.531 z_b^2 H u_{xx}\right]_t + \left[z_b H (hu)_{xx}\right]_t, \tag{17}$$

$$P_2 = (Hv)_t + \left[0.531 z_b^2 H v_{yy}\right]_t + \left[z_b H (hv)_{yy}\right]_t. \tag{18}$$

The remaining terms, unused in Equation (17), are multiplied by Equation (16) and grouped as:

$$\Psi_{P_1} = \frac{z_b^2}{2} u_{xx} + z_b (hu)_{xx}, \tag{19}$$

$$\Psi_{P_2} = \frac{z_b^2}{2} v_{yy} + z_b (hv)_{yy}. \tag{20}$$

It should be noted that most Boussinesq-type equations (BTEs) involve time-dependent terms with this challenging structure. Alternative methods, such as those presented by Antuono et al. [51], may simplify implementation, particularly for finite volume schemes.

Equations (11) and (12) use spatially moving pressure disturbances. The ship's hull form is predetermined at the start of the calculation. The wave creation from the moving pressure terms may take place simultaneously with other wave-producing functions, such as a wave-maker source for spectral or monochromatic waves.

2.3. Governing Equations for Inner Domain

The governing equation for the inner domain is defined as:

$$\nabla^2 \phi = 0. \tag{21}$$

Kinematic and dynamic boundary conditions on the dynamic free surface are both written as follows:

$$\frac{\partial \phi}{\partial z} = \frac{\partial \eta}{\partial t} + \frac{\partial \phi}{\partial \tau} \frac{\partial \eta}{\partial x}, \tag{22}$$

$$g\eta = -\frac{\partial \phi}{\partial \tau} - \frac{1}{2} (\nabla \phi)^2. \tag{23}$$

These boundary conditions can be rewritten using a semi-Lagrangian framework:

$$\frac{D\eta}{D\tau} = \frac{\partial \phi}{\partial y} - \frac{\partial \phi}{\partial x} \frac{\partial \eta}{\partial x}, \tag{24}$$

$$\frac{D\phi}{D\tau} = -g\eta - \frac{1}{2} (\nabla \phi)^2 + \frac{D\eta}{D\tau} \frac{\partial \phi}{\partial y}, \tag{25}$$

where $\frac{D}{D\tau} = \frac{\partial}{\partial \tau} + \mathbf{v}_p \cdot \nabla$, and $\mathbf{v}_p = (0, D\eta/D\tau)$. These equations have been solved using a finite volume approach for simulating two-dimensional nonlinear wave behavior. This study applies a similar methodology to simulate in the inner domain. The fundamental feature of the semi-Lagrangian form is that the node's horizontal coordinate is fixed, but it is free to move vertically.

2.4. Governing Equations for Matching Domain

The contacts between the inner and outer domains are four in number. The volume flux is used to specify the matching conditions for interfaces:

$$\Psi_j(i) = \int_{y_j(i)}^{-h} u_j(i) dy, \quad j = 1, 2, 3, 4. \tag{26}$$

And the stream function of each node on the matching interfaces, which defines the inner domain solution, is $\Psi_j(i)$. Each interface node's vertical location beneath the free surface is represented as:

$$z(i) = \eta - \frac{(h+\eta)}{(N-1)}(i-1), \quad i = 1, 2, 3, ...N \tag{27}$$

where N represents the number of nodes oriented vertically. The surface height of the water waves at the corresponding boundary contacts defines the outer domain solution. The horizontal velocity, $u_j(i)$, is defined for interfaces of the outer domain and is defined by the fourth order polynomial

$$u(i) = \bar{u} - \frac{1}{2}\left[(h+z(i))^2 - \frac{(h+\eta)^2}{3}\right]\bar{u}_{xx} + \frac{1}{24}\left[(h+z(i))^4 - 2(h+z(i))^2(h+\eta)^2\right]\bar{u}_{xxxx}. \tag{28}$$

The matching conditions on the interfaces are described for continuations of volume flux:

$$\bar{u}_j = \frac{\Psi_j}{(h+z_j)}, \quad j = 2, 3. \tag{29}$$

Then, the equality of the water wave surface elevation is defined as $\eta_j = z_j$, which is determined by the solution of the inner domain.

2.5. Moored Ship Motion

In order to limit the analysis to the scenario where the ship's forward speed is zero, the motion of a moored ship must be mathematically formulated. Both incoming waves and waves scattered by the floater's presence contribute to wave forces.

$$\nabla^2\varphi_s = 0 \quad \text{within the fluid domain,} \tag{30}$$

$$\frac{\partial^2\varphi_s}{\partial\tau^2} + g\frac{\partial\varphi_s}{\partial z} = 0 \quad \text{on} \quad z = 0, \tag{31}$$

$$\frac{\partial\varphi_s}{\partial\nu} = -\frac{\partial\varphi_I}{\partial\nu} - \left(\frac{\partial\mathbf{x}}{\partial\tau} + \boldsymbol{\alpha}\times\mathbf{r}_b\right)\cdot\nu, \quad \text{on } S, \tag{32}$$

$$\varphi_s = 0 \quad \text{at } z = -h \text{ or } r = R, \tag{33}$$

where φ_s represents the scattering potential and φ_I represents the potential due to incoming waves; $\mathbf{x}$ describes translational displacements and $\boldsymbol{\alpha}$ denotes rotational displacements. The boundary conditions incorporate normal vectors, $\boldsymbol{\nu}$, radius, R, and surface, S, for numerical computations. In the case where a moored ship is floating in still water, its center of gravity is denoted by $G(x_g, y_g, z_g)$. The dynamic response of the ship to external forces and hydrodynamic interactions can be expressed in terms of its six degrees of freedom, which describe both translational and rotational motions.

The motion of the ship in the j^{th} mode is mathematically represented as:

$$S_j = A_{i,j}\exp(-i\omega t), \quad j = 1, 2, 3, ..., 6. \tag{34}$$

Here, S_j, where $j = 1, 2, \ldots, 6$, represents the generalized displacement components of the ship's motion. The indices $j = 1, 2, 3$ correspond to the translational displacement modes—heave, sway, and surge—whereas $j = 4, 5, 6$ correspond to the rotational displacement modes—roll, pitch, and yaw, respectively. Each mode describes a fundamental aspect of the ship's dynamic behavior in response to external forces such as waves, currents, and mooring constraints.

The wave-induced oscillation of the j^{th} mode is characterized by the wave amplitude, A_j, which determines the intensity of the response under varying environmental conditions. By analyzing these motion components, the stability and dynamic characteristics of the moored ship can be systematically evaluated, leading to improved predictions of harbor resonance effects and mooring safety.

2.6. Numerical Solution of Finite Volume Method

The current Boussinesq-type formulation integrates numerical methods that preserve conservative properties, ensuring stability and accuracy in wave modeling. This approach inherently contains the nonlinear shallow-water equations (NSWEs) as a subset, making it suitable for analyzing complex hydrodynamic scenarios.

Building on previous research, the BOSZ model employs a hybrid numerical approach, where hydrostatic components are resolved using a finite volume method (FVM), while the non-hydrostatic pressure correction terms are handled via a central differential finite difference method (FDM). This combination allows for a more accurate representation of wave dynamics, particularly in shallow-water regions.

The finite volume method estimates the spatial derivatives of flow and bed slope terms through an advanced solution strategy based on the Harten–Lax–van Leer-contact (HLLC) approximate Riemann solver. This solver is applied across all cell interfaces to ensure precise calculation of flux terms and to maintain stability in wave propagation simulations. To enhance accuracy, a two-dimensional constrained reconstruction technique, as described by Kim et al. [52], is utilized to provide the input states for the Riemann solver at each side of the computational grid cells. The method employs a fourth-order wave-number extended and oscillation-controlled reconstruction, effectively mitigating numerical diffusion and enhancing the resolution of wave structures.

The governing equations, previously introduced in Equations (9)–(12), can be reformulated into a conservative expression as follows:

$$\frac{\partial U}{\partial t} + \nabla \cdot (F(U^*) + G(U^*)) = S(U^*), \quad \Omega \times [0,t] \subset R^2 \times R^+, \tag{35}$$

where the source term is defined as $S(U) = S_b + S_d$, incorporating both the bottom slope contribution S_b and the dispersive term S_d. The flux vectors F and G capture the nonlinear characteristics of the governing equations, playing a crucial role in accurately simulating wave dynamics and their interaction with coastal structures.

$$\begin{aligned} U &= \begin{bmatrix} H \\ P \\ Q \end{bmatrix}, \quad F(U^*) = \begin{bmatrix} Hu \\ Hu^2 + \frac{1}{2}gH^2 \\ Huv \end{bmatrix} \quad G(U^*) = \begin{bmatrix} Hv \\ Huv \\ Hv^2 + \frac{1}{2}gH^2 \end{bmatrix} \\ S_b &= \begin{bmatrix} 0 \\ -gH\frac{\partial z_b}{\partial x} - \frac{1}{\rho}H\frac{\partial P_e}{\partial x} \\ -gH\frac{\partial z_b}{\partial y} - \frac{1}{\rho}H\frac{\partial P_e}{\partial x} \end{bmatrix} \quad S_d = \begin{bmatrix} -\Psi_c \\ -u\Psi_c + \Psi_{mx} \\ -v\Psi_c + \Psi_{my}, \end{bmatrix} \end{aligned}$$

For computational reasons, in this report we use $H = q_1$, $Hu = q_2$, and $Hv = q_3$, then $q = [q_1, q_2, q_3]^T$; the above equations in the equivalent form are as follows:

$$
\begin{aligned}
U(q) &= \begin{bmatrix} H \\ Hu \\ Hv \end{bmatrix} = \begin{bmatrix} q_1 \\ q_2 \\ q_3 \end{bmatrix}, \quad F(q) = \begin{bmatrix} q_2 \\ \frac{q_2^2}{q_1} + \frac{1}{2}gq_1^2 \\ \frac{q_3 q_2}{q_1} \end{bmatrix}, \quad G(q) = \begin{bmatrix} q_3 \\ \frac{q_3 q_2}{q_1} \\ \frac{q_3^2}{q_1} + \frac{1}{2}gq_1^2 \end{bmatrix} \\
S_b &= \begin{bmatrix} 0 \\ -gq_1 \frac{\partial z_b}{\partial x} - H\frac{1}{\rho}\frac{\partial P_e}{\partial x} \\ -gq_2 \frac{\partial z_b}{\partial y} - H\frac{1}{\rho}\frac{\partial P_e}{\partial x} \end{bmatrix}, \quad S_d = \begin{bmatrix} -\Psi_c \\ -u\Psi_c + \Psi_{mx} \\ -v\Psi_c + \Psi_{my}, \end{bmatrix}
\end{aligned} \tag{36}
$$

$$
\begin{aligned}
P_1 &= Hu + H\left[\frac{z_b^2}{2}\left(\frac{\partial^2 u}{\partial x^2} + \frac{\partial^2 v}{\partial y \partial x}\right) + z_b\left(\frac{\partial^2 (hu)}{\partial x^2} + \frac{\partial^2 (hv)}{\partial y \partial x}\right)\right], \\
P_2 &= Hv + H\left[\frac{z_b^2}{2}\left(\frac{\partial^2 u}{\partial x \partial y} + \frac{\partial^2 v}{\partial y^2}\right) + z_b\left(\frac{\partial^2 (hu)}{\partial x \partial y} + \frac{\partial^2 (hv)}{\partial y^2}\right)\right], \\
\Psi_c &= u\left\{\left[\left(\left(\frac{z_b^2}{2} - \frac{h^2}{6}\right)h\left(\frac{\partial u}{\partial x} + \frac{\partial v}{\partial y}\right)_x + \left(z_b + \frac{h}{2}\right)h\left(\frac{\partial (hu)}{\partial x} + \frac{\partial (hv)}{\partial y}\right)\right)_x\right]_x \right. \\
&\quad \left. + \left[\left(\left(\frac{z_b^2}{2} - \frac{h^2}{6}\right)h\left(\frac{\partial u}{\partial x} + \frac{\partial v}{\partial y}\right)_y + \left(z_b + \frac{h}{2}\right)h\left(\frac{\partial (hu)}{\partial x} + \frac{\partial (hv)}{\partial y}\right)\right)_y\right]_y\right\}, \\
\Psi_{my} &= H_t\left[\frac{z_b^2}{2}\left(\frac{\partial^2 u}{\partial x \partial y} + \frac{\partial^2 v}{\partial y^2}\right) + z_b\left(\frac{\partial^2 (hu)}{\partial x \partial y} + \frac{\partial^2 (hv)}{\partial y^2}\right)\right], \\
\Psi_{mx} &= H_t\left[\frac{z_b^2}{2}\left(\frac{\partial^2 u}{\partial x^2} + \frac{\partial^2 v}{\partial x \partial y}\right) + z_b\left(\frac{\partial^2 (hu)}{\partial x^2} + \frac{\partial^2 (hv)}{\partial x \partial y}\right)\right].
\end{aligned}
$$

The governing Boussinesq-type equation incorporates both hyperbolic and parabolic terms to describe the flow and dispersion processes. The parameter z_b, representing the reference depth, serves as a free variable that can be adjusted to optimize dispersion characteristics for specific applications, particularly influencing the parabolic term. Nwogu (1993) determined an optimal value of $z_b = -0.531h$ for simulating wind-generated waves by aligning the phase velocity derived from the linearized governing equations with Airy wave theory, ensuring accuracy for wave depths satisfying $kh < \pi$, where k denotes the wave number. The terms $F(U^*)$ and $G(U^*)$, which encapsulate the homogeneous component of the nonlinear shallow-water equations (NSWEs) with enhanced surface gradient terms, are computed using the finite volume method via the Riemann solver. Meanwhile, the local acceleration and source terms appearing in Equation (35) are handled through a finite difference approach:

$$
S(U^*) = \begin{bmatrix} \Psi_c \\ -gH\frac{\partial z_b}{\partial x} - u\Psi_c - H\frac{1}{\rho}\frac{\partial P_e}{\partial x} - \Psi_P\frac{\partial H}{\partial t} - \Psi_{P_1}H + \Psi_{mx} \\ gH\frac{\partial z_b}{\partial y} - u\Psi_c - H\frac{1}{\rho}\frac{\partial P_e}{\partial y} - \Psi_Q\frac{\partial H}{\partial t} - \Psi_{P_2}H + \Psi_{my} \end{bmatrix}. \tag{37}
$$

The form of a pressure disturbance that creates ship-borne waves is described by the ψ_S terms in Equations (11), (12), and (37). Despite the fact that the pressure field might take on several forms, the formulations proposed by Bayraktar and Beji [46] are used in this work. While Equation (39) represents a longer, more ship-like pressure distribution, Equation (38) represents a hemispherical pressure distribution. These forms have the following spatial definitions:

$$(\psi_S)_{ij} = D_p \sqrt{1 - \left(\frac{x_i^2 + y_j^2}{r^2}\right)}, \quad \text{(Hemispherical Shape)} \tag{38}$$

$$(\psi_S)_{ij} = D_p \left[1 - c_L \left(\frac{x_i}{L_p}\right)^4\right] \left[1 - c_B \left(\frac{y_j}{B_p}\right)^2\right] e^{-a\left(y_j/B_p\right)^2}, \quad \text{(Elongated Ship-Like Shape)} \tag{39}$$

The pressure distribution's length, width (as measured from the longitudinal center axis), and draft are shown above by the letters L_p, B_p, and D_p. The hemispherical shape's radius is denoted by the parameter r. In this case, the form parameters a, c_L, and c_B are set to 16, 2, and 2, respectively.

Furthermore, non-hydrostatic components from the orthogonal velocity components with cross-space and time derivatives are included in the momentum equations and are handled independently. Here, we repeat the xyt cross terms from Equations (14) and (15) as:

$$\begin{aligned} \Psi_{p_2} &= \tfrac{z_b^2 v_{xyt}}{2} + z_b (hv)_{xyt} \\ \Psi_{Q_2} &= \tfrac{z_b^2 u_{xyt}}{2} + z_b (hu)_{xyt}. \end{aligned} \tag{40}$$

First-order upwind discretization of the u_t and v_t time-derivatives is used to evaluate them by utilizing stored variables from the current and previous time steps. In this study, the Courant number is fixed at 0.5 for every test. Each time step starts with a calculation of the time step size, which can change based on the flow circumstances to ensure that the Courant constraint is never broken. The expression for D_p in Equations (38) and (39) is $D_s \cdot 10^5$, where D_s is the ship draft and $1\,\text{bar} = 10^5\,\text{N/m}^2 = 10^5\,\text{kg/ms}^2$.

1. Satisfying the boundary condition on the floater surface,

$$\frac{\partial \Phi_s}{\partial n} = -\frac{\partial \Phi_I}{\partial n} - \left(\frac{\partial \mathbf{X}}{\partial \tau} + \boldsymbol{\omega} \times \mathbf{R}_b\right) \cdot \mathbf{n}, \tag{41}$$

   where Φ_s is the scattered velocity potential, Φ_I represents the incident velocity potential, $\mathbf{X}$ and $\boldsymbol{\omega}$ denote translational and rotational displacements, $\mathbf{R}_b$ is the vector from the body's center to the surface, and $\mathbf{n}$ is the outward-pointing unit normal.

2. Computing second-order drift forces,

$$\begin{aligned} F_k^{(2)} = \gamma g \int_{W_l} \eta\, \mathbf{Q}\, dl + \gamma \int_{S_f} \left(\nabla \Phi^{(1)} \cdot \nabla \Phi^{(1)}\right) dS \\ - \int_{S_f} P_I^{(1)} \mathbf{n}^{(1)}\, dS, \end{aligned} \tag{42}$$

   where $F_k^{(2)}$ represents second-order wave forces, η is the wave elevation, W_l is the mean waterline, $\Phi^{(1)}$ is the first-order potential, $P_I^{(1)}$ is the first-order pressure, and $\mathbf{n}^{(1)}$ is the perturbed normal vector.

The pressure contribution from incident waves is used to evaluate the forces exerted on the floater. These forces include the impact of low-frequency components and their interaction with scattered waves, enabling an accurate simulation of the floater's hydrodynamic behavior.

2.7. Boundary Conditions

1. For the boundary condition for partial absorption on the harbor wall, the boundary requirement for partial absorption is:

$$\frac{\partial \psi_l}{\partial n} = -ika\psi_l, \quad l = 0, 1, \ldots, 6. \tag{43}$$

2. The zero-flux boundary condition on the seabed is written as:

$$\frac{\partial \psi_l}{\partial n} = 0. \tag{44}$$

3. For rthe ship surface boundary condition on the ship surface, S_0, the boundary condition is given by:

$$\frac{\partial \psi_l}{\partial n} = -\frac{\partial \psi_{\text{inc}}}{\partial n}. \tag{45}$$

For the incident wave propagating at an angle θ_{inc} with respect to the x-axis, the velocity potential is:

$$\Psi_{\text{inc}}(x, y, z, t) = \Re\left[\frac{A_0\omega}{ig}\phi_{\text{inc}}\frac{\cosh k(z+h)}{\cosh kh}e^{-i\omega t}\right], \tag{46}$$

with

$$\psi_{\text{inc}} = \sum_{n=0}^{\infty} i^n \epsilon_n J_n(kr)\cos n(\theta - \theta_{\text{inc}}), \tag{47}$$

where J_n is the n-th order Bessel function of the first kind, A_0 is the wave amplitude, θ is the angular variation, and $\epsilon_n = 2$ for $n > 0$ ($\epsilon_0 = 1$). With the addition of matching criteria at interfaces between various regions, the scattered wave potential, Ψ_s, fulfills boundary conditions that are comparable to those of the incident wave potential.

Variables from the Boussinesq equations are transformed to determine the pressure and fluid particle velocities on the floater's surface. Calculating wave-induced forces and floater motion requires these parameters. It is essential to comprehend the forces that wave action exerts on moored ships in order to evaluate their motion and stability in harbor situations. The integration of the pressure field throughout the ship's wetted surface yields these forces. The following is how the linearized Bernoulli equation is used to obtain the pressure field itself:

$$P = -\rho\left(\frac{\partial \Psi}{\partial t} + gz\right) = -\rho\left(\sum_{j=1}^{6}\zeta_j\psi_j e^{i\omega t} + \psi_0\right) - \rho g z, \tag{48}$$

where Ψ represents the velocity potential, z is the vertical position, ρ is the density of the fluid, ω is the wave frequency, and ζ_j are modal amplitudes. The dynamic component of the hydrodynamic force is computed as an integral over the ship's wetted surface, denoted as S_0:

$$F_{\text{Dyn}} = \int_{S_0}\sum_{j=1}^{6}\zeta_j\mathcal{F}_{ij}e^{i\omega t}\,\mathrm{d}s, \quad i = 1, \ldots, 6, \tag{49}$$

where the coefficients $\mathcal{F}_{ij}$ are expressed as:

$$\mathcal{F}_{ij} = -\rho\int_{S_0}\frac{\partial \psi_j}{\partial \mathbf{n}}\,\mathrm{d}s = \omega^2 A_{ij} - i\omega B_{ij}. \tag{50}$$

In this formulation, A_{ij} and B_{ij} represent the added mass and damping terms, respectively, while $\partial\psi_j/\partial\mathbf{n}$ is the derivative of the velocity potential normal to the surface. The buoyancy or hydrostatic force is evaluated as:

$$F_{\text{Hydro},i} = -\rho g \int_{S_0} \psi_0 z \, \mathrm{d}s, \quad i = 1, \ldots, 6, \tag{51}$$

where g is gravitational acceleration and ψ_0 corresponds to the static velocity potential component. Wave-induced forces are described as:

$$F_{\text{Exc},i} = \text{Re}\{\mathcal{X}_i e^{i\omega t}\}, \quad i = 1, \ldots, 6, \tag{52}$$

with

$$\mathcal{X}_i = -\rho \int_{S_0} \frac{\partial \psi_0}{\partial \mathbf{n}} \, \mathrm{d}s. \tag{53}$$

The governing equations for ship motion in six degrees of freedom (6-DOF) are obtained in the finite volume framework. The equation of motion can be expressed in the following generic form:

$$\sum_{j=1}^{6} \left[(\mathcal{M}_{ij} + A_{ij}) \frac{\partial^2 \eta_j}{\partial t^2} + B_{ij} \frac{\partial \eta_j}{\partial t} + C_{ij} \eta_j \right] = F_{\text{Exc},i}, \quad i = 1, \ldots, 6, \tag{54}$$

where $\mathcal{M}_{ij}$ are coefficients for the ship's inertia, A_{ij} and B_{ij} are added mass and damping terms, C_{ij} are restoring coefficients due to buoyancy, and η_j are displacements for each mode of motion. The amplitude of ship response, ζ_i, is then evaluated as:

$$\zeta_i = \frac{F_{\text{Exc},i}}{-\omega^2(\mathcal{M}_{ij} + A_{ij}) + i\omega B_{ij} + C_{ij}}, \quad i = 1, \ldots, 6. \tag{55}$$

The response function, linking excitation forces to the dynamic response, is expressed as:

$$T^s(\omega) = \left[-(\mathcal{M}_{ij} + A_{ij})\omega^2 + i\omega B_{ij} + C_{ij} \right]^{-1}. \tag{56}$$

The wave excitation force in the finite volume context for a harbor environment is given below as:

$$F_{\text{Exc},0} = T(\omega, \theta_{\text{inc}}) A_0, \tag{57}$$

where the wave frequency, angle of incidence, and amplitude are denoted by ω, θ_{inc}, and A_0, respectively. In the harbor domain, the wave excitation transfer function is denoted by the expression $T(\omega, \theta_{\text{inc}})$. The results of Takagi et al. (1993) and Yoo (1998) [37,38] are contrasted with the increased mass and damping coefficients calculated using the numerical approach. The definition of the dimensionless additional mass coefficient are defined as:

$$A_{ij}/M \quad \text{for } i, j = 1, 2, 3, \quad \text{and } A_{ij}/ML^2s^2 \quad \text{for } i, j = 4, 5, 6,$$

and the dimensionless damping coefficients were defined as:

$$B_{ij}/M\omega L_s^2 \quad \text{for } i, j = 1, 2, 3, \quad \text{and } B_{ij}/M\omega L_s^3 \quad \text{for } i, j = 4, 5, 6,$$

where M and ω represent the moored ship's mass and frequency, respectively.

2.8. Von Neumann Stability Analysis

The stability of the numerical scheme used to solve Nwogu's depth-integrated nonlinear coupled Boussinesq-type equations is critical to ensure accurate and reliable simulations.

The hybrid finite volume method (FVM) and finite difference method (FDM) employed in this study require careful stability analysis to prevent numerical instabilities and ensure convergence. To analyze the stability of the numerical scheme, we employ the Von Neumann method, which examines the growth of Fourier modes in the discretized equations. Considering a linearized form of the governing equations, the solution is expressed as a Fourier series:

$$u_j^n = \hat{u} e^{i(kj\Delta x)} e^{\sigma n \Delta t}, \tag{58}$$

where k is the wave number, Δx and Δt are the spatial and temporal step sizes, and σ represents the amplification factor. Applying the hybrid FVM–FDM scheme to the linearized equations and substituting the Fourier mode representation, we derive the amplification factor $G = e^{\sigma \Delta t}$. Stability is ensured if

$$|G| \leq 1. \tag{59}$$

Through detailed derivations, we obtain the Courant–Friedrichs–Lewy (CFL) condition:

$$\frac{C\Delta t}{\Delta x} \leq \alpha, \tag{60}$$

where C is the characteristic wave speed and α is a stability coefficient dependent on the numerical scheme's order of accuracy, which lie between 0 and 1.

$$\Delta t = min\left(\frac{C\Delta x}{\mid u_i \mid + \sqrt{gh_i}}, \frac{C\Delta y}{\mid v_j \mid + \sqrt{gh_j}}, \Delta T \right) \tag{61}$$

2.9. Slope Limiter

To further enhance stability, a TVD limiter is applied to prevent spurious oscillations in steep gradients. The TVD condition ensures that numerical oscillations do not grow in magnitude, contributing to the overall stability of the scheme. The limiter function $\Phi(r)$ is selected, such that:

$$0 \leq \Phi(r) \leq 2, \tag{62}$$

where r is the ratio of consecutive gradient differences.

2.10. Numerical Verification

A grid refinement study is conducted to verify stability by analyzing the error norm $||u^{n+1} - u^n||$ over different resolutions. The results confirm that the numerical scheme remains stable under the derived CFL condition, with negligible numerical dissipation and dispersion effects. The numerical implementation of the present study involves solving 2D time-dependent Nwogu's depth-integrated nonlinear coupled Boussinesq-type equations (NCBTEs) using a hybrid finite volume method (FVM) and finite difference method (FDM). This approach is particularly suited for capturing nonlinear dispersive wave forces acting on a fixed ship within complex harbor geometries and varying depths.

The flux at the intercell is predicted using the HLLC Riemann solver. The flux is computed using cell face reconstruction, which is anticipated by the cell slope limiter, and the corrected value in the cell center is $U_i^{n+1/2}$.

$$UM_{i+1/2}^n = U_i^n + \frac{1}{2}\phi(r)(U_i^n - U_{i-1}^n) \tag{63}$$

Equation (32) is reconstructed using the cell boundary vector, calculated with the predicted cell center:

$$U_i^{n+1/2} = U_i^n + k_x\left(F(U^* M_{i+1/2}^n) - F(U^* M_{i-1/2}^n)\right) + \ldots$$
$$k_y\left(G(U^* M_{j+1/2}^n) - G(U^* M_{j-1/2}^n)\right) + S(U_i^*)\frac{\Delta t}{2}, \tag{64}$$

where $k_x = \frac{\Delta t}{2\Delta x}$ and $k_y = \frac{\Delta t}{2\Delta y}$ are wave number x-axis and y-axis, respectively. We use the Riemann flux solve with finite volume method [47].

3. Results

3.1. Convergence Analysis

The convergence and error analysis of the current numerical method includes the ship in the middle of the rectangular region. The measurements of the ship and the rectangular domain are identical to those found in the validation section. Using the least-squares method, the convergence rate of the mesh models in the rectangle domain is determined. The error norm formula for the domain discretized into M_1 and M_2 mesh elements is as follows:

$$\begin{aligned} \text{Error}_{M_1}: \quad & \frac{\|\Psi_{M_1} - \Psi_{M_\infty}\|_2}{B} = M_1^{-\alpha}, \\ \text{Error}_{M_2}: \quad & \frac{\|\Psi_{M_2} - \Psi_{M_\infty}\|_2}{B} = M_2^{-\alpha}. \end{aligned} \tag{65}$$

In this context, α represents the order of convergence, while B denotes the error constant. The solution corresponding to a discretized domain with M_i elements is given by $\phi_{M_i}, i = 1, 2, 3, \ldots$. Throughout the computations, the value Ψ_{M_∞} is approximated as Ψ_{M_3}. The parameters α and B are determined by solving the two equations given in Equation (65). The computational domain is discretized using unstructured linear triangular elements, with mesh refinements consisting of 1225, 2450, and 4700 elements. Once the equations in Equation (65) are solved, the order of convergence is evaluated.

As the number of grid points rises, the accuracy of the current technique falls, as seen in Figure 2. Figure 2 provides the logarithmic error norm for Paradip Port with respect to logarithmic segment division. For Paradip Port, the order of convergence is 1.57. The numerical scheme's inaccuracy drastically decreases as the segment division rises. As a result, the implementation of the numerical system is verified.

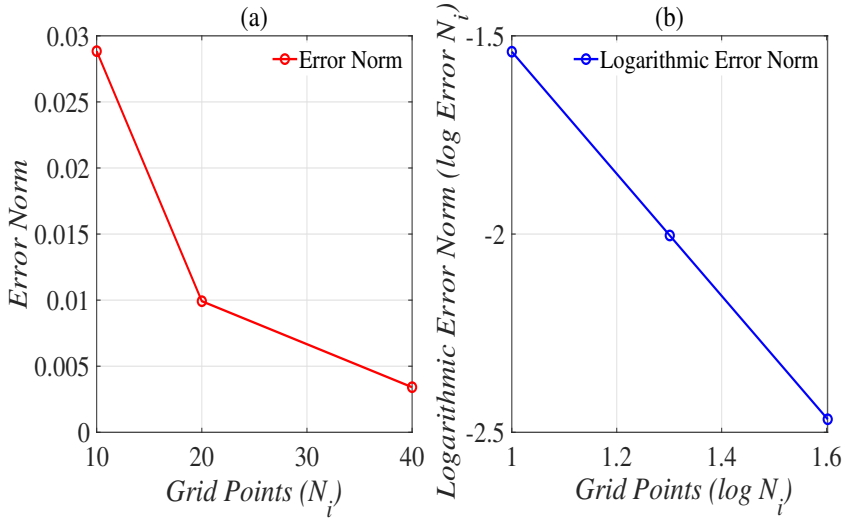


Figure 2. The logarithmic error with (**a**) logarithmic border segment division and (**b**) error norm with segment division provide the convergence of present FVM.

3.2. Validation Results

The rectangular harbor domain, whose dimensions are 1.5 m for length (L), 0.9 m for width (B), and 0.15 m for depth (H) is chosen in order to test the numerical method for the motion of a moored ship. A moored ship is represented using a rectangular body with specified dimensions, draft (D_s), depth (H_s), width (B_s), and length (L_s), which are set to 0.3 m, 0.12 m, 0.09 m, and 0.06 m, respectively. The rectangular body is centrally placed within the rectangular harbor, with its sides aligned parallel to the harbor boundaries.

The variation of heave-added mass and heave-damping coefficients as functions of the dimensionless frequency $\omega^2 L_s/g$ is illustrated in Figure 3a,b. Similarly, Figure 3c,d present the sway-added mass and damping coefficients in relation to the dimensionless frequency. The results obtained from the present numerical model exhibit strong agreement with those from previous numerical approaches. The frequency interval employed in the current numerical simulations is set to 0.05.

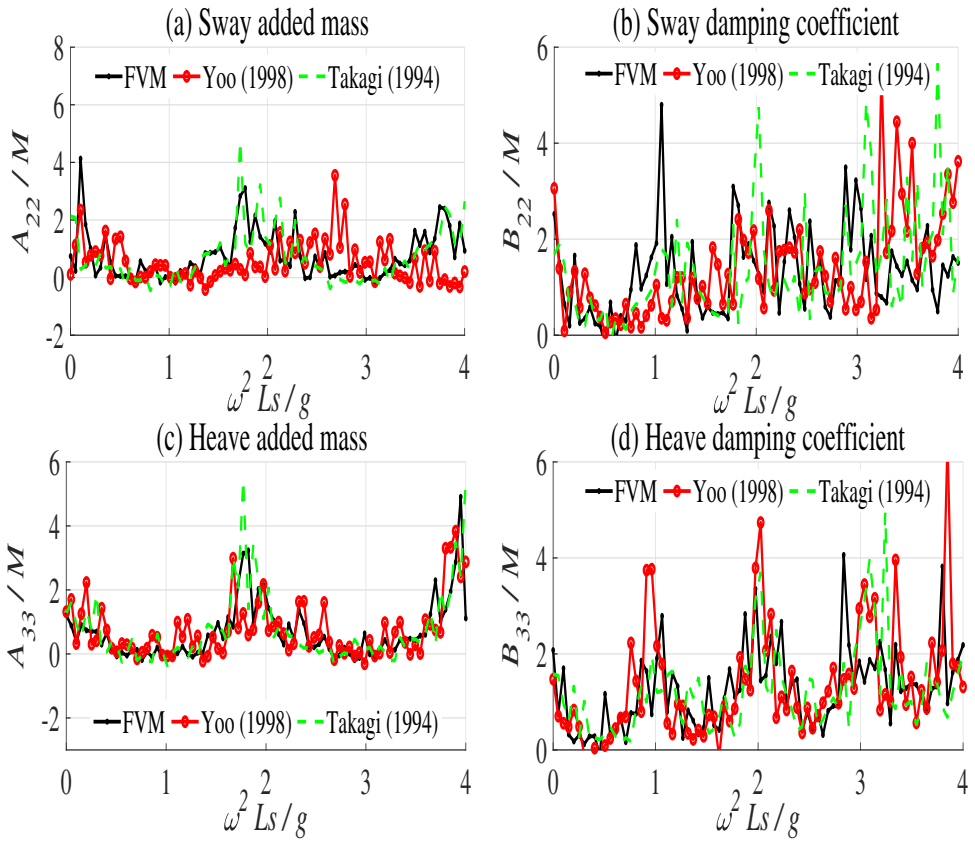


Figure 3. Comparison of FVM scheme with the previous numerical scheme by Takagi [37] and Yaoo [38] for validation of the current scheme.

3.3. Numerical Simulation Results

The waves produced by moving pressure fields are the focus of the numerical simulations for Nwogu's 2D depth integrated NCBTEs. These simulations are carried out for two distinct surface pressure functions: a moored ship-like form, which is an elongated-shaped pressure field, and a hemispherical pressure field, which is a slender-body type pressure field.

3.4. Hemispherical and Elongated Ship-like Shape Pressure Forcing

A hemispherical pressure field is defined in Equation (21). The numerical rectangular simulation region is considered 600 m $\times$ 300 m with D_p. Here, D_p is the peak value of

the pressure distribution, which is defined at $x = 0, y = 0$, and r is the radius of the hemispherical pressure field.

The time step is taken as Δt. Figure 4 shows the water wave surface elevation contours for a moving hemispherical pressure field at time steps $\Delta t = 0.2$ using NCBTE models with different Froude number values, $F_r = 0.1, 0.6, 1.2$. This is the simulated wave field at the pressure field speed or depth-based Froude number, Fr. The wedge angle of 58, which was obtained from the simulated wave field at 48 s, is demonstrated to be a reasonable approximation of the theoretical value.

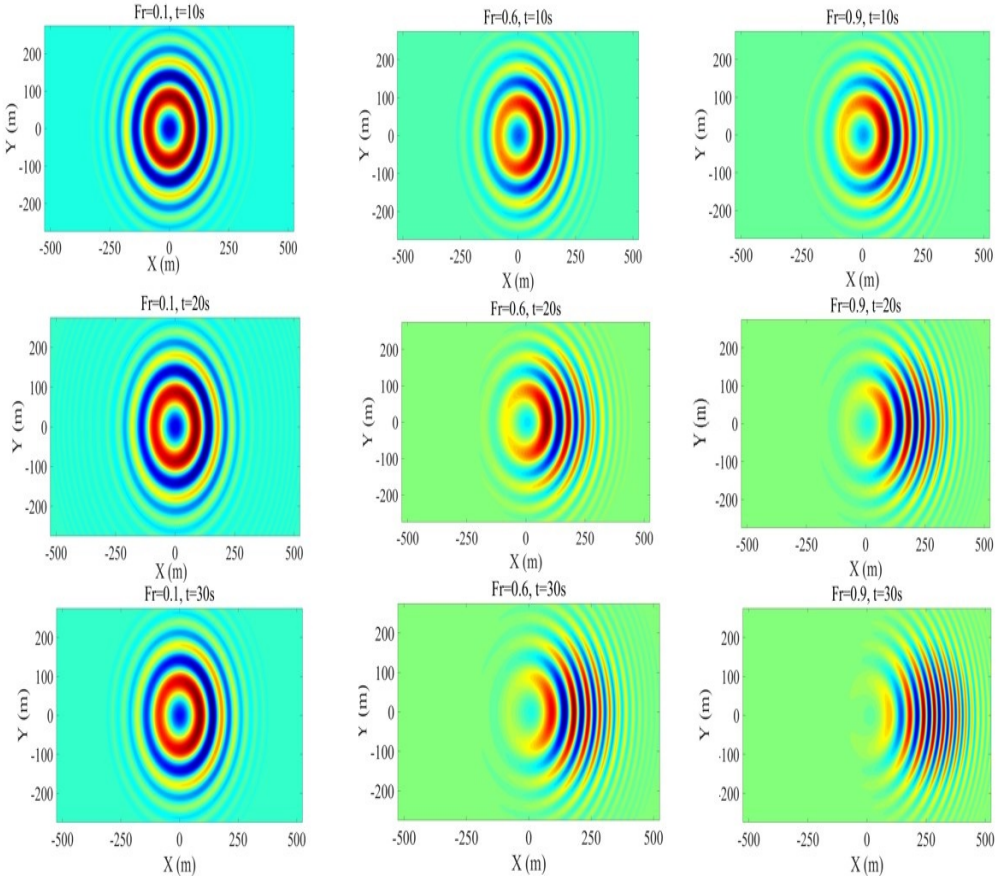


Figure 4. Water wave surface elevation contours for a moving hemisphere pressure field at time steps $\Delta t = 0.2$ using NCBTE models with different Froude number values, $F_r = 0.1, 0.6, 0.9$, with different time, t = 10 s, 20 s, 30 s.

Figure 5 shows the water wave surface elevation contours for a moored ship-like form as an elongated-shaped pressure field at different time, t = 10, 20, 30, using NCBTE models with different Froude number values, $F_r = 0.1, 0.6, 1.2$, respectively. In this case, the peak pressure value, D_p, is set at 3000 and is reached at $\Delta t = 0.25$. The length is denoted by L_p, the breadth by B_p, and the shape constants are defined by a, c_B, and c_L, which are set to 16, 2, and 16, respectively.

Only at $x = 0, y = 0$ is the elongated-shaped pressure field defined, and it is set to zero outside these areas. The numerical simulation's rectangular area is 600 m $\times$ 300 m, with a time step of $\Delta t = 0.25$ and grid size of $\Delta x = 0.2 = \Delta y$. The water depth in the simulations is $h = 20$ m, and the length to beam ratio is 0.4. The primary distinctions between sub-critical and super-critical Froude numbers are discussed here, along with the wave patterns generated by various types of moving surface pressure. The wedge and propagation angle results show that the influence of divergent waves increases with

decreasing Froude number, and the position of transverse waves, at crest or trough, changes with ship velocity.

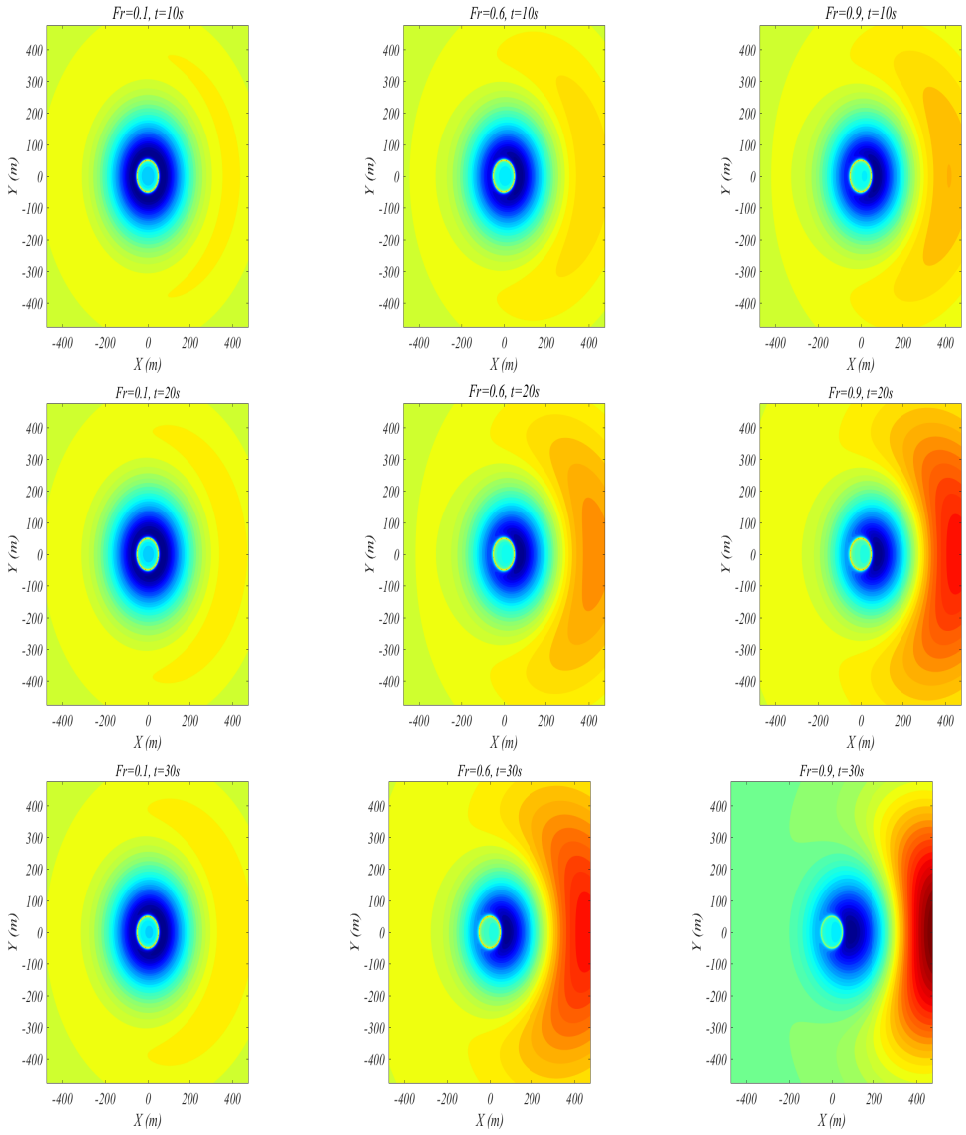


Figure 5. Water wave surface elevation contours for a moving elongated-shaped pressure field at time steps $\Delta t = 0.2$ using NCBTE models with different Froude numbers, $F_r = 0.1, 0.6, 0.9$, with different time, t = 10 s, 20 s, 30 s.

Figure 6 shows the wave force and the surface elevation, defined here with respect to time. The water wave surface elevation at an incident wave angle exhibits a greater wave amplitude within the domain. The time series representing the forces exerted by incident waves on the ship were derived by utilizing the time series of free wave elevation estimated for a specific point in the vicinity of the ship's mooring location, in conjunction with the outcomes from the frequency-domain diffraction analysis concerning bow waves. Due to the constraints associated with the method employed to obtain the force time series, which relies on fast Fourier transform, it is advisable to consider only the initial 500 s of the free-surface elevation time series. Figure 6 illustrates the time series of the wave-induced force applied to the ship by the incident waves. It also highlights another limitation of the implemented procedure for calculating the time series: oscillations in the force time series are observed prior to the arrival of the incident wave at the mooring site (approximately at t = 90 s), which is not physically feasible.

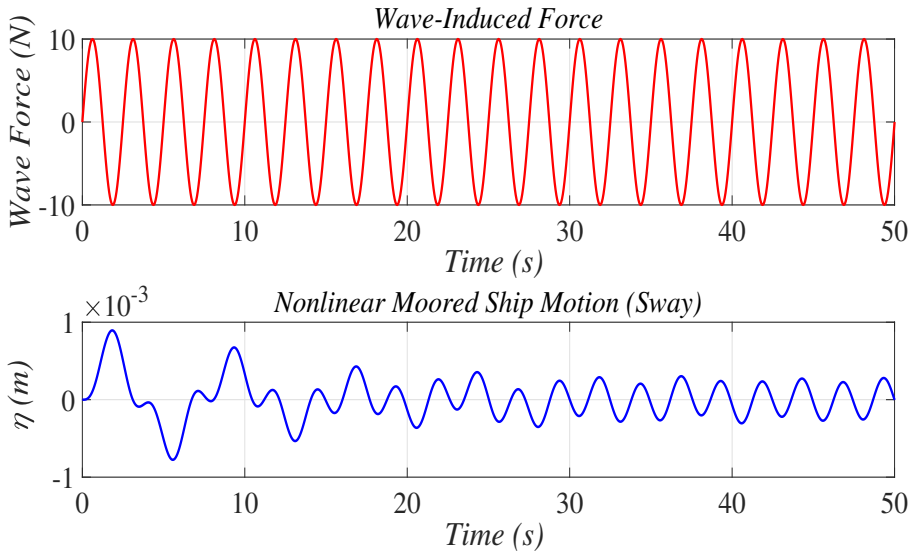


Figure 6. Wave−induced force and surface elevation are defined with respect to time (sec).

Figure 7 shows the surge, sway, and yaw motions of a moored ship in a harbor due to external forces with wind waves, which is defined in Equation (55). Wind-induced effects typically influence surge, sway, and yaw motions more significantly. The surge motion represents the forward and backward movement of the ship along its longitudinal axis. Figure 7 shows a relatively small fluctuation initially, followed by a more pronounced oscillation towards the end of the time period, possibly due to increased water wave wind effects. The sway motion indicates the lateral movement of the ship, perpendicular to its length. It exhibits minor fluctuations at the start, with a more significant variation in the latter stages, suggesting an increase in external forcing or ship response. The yaw motion (green line) represents the rotational movement of the ship about its vertical axis and continuous increase in yaw angle over time, indicating a gradual turning effect, likely caused by asymmetric wind.

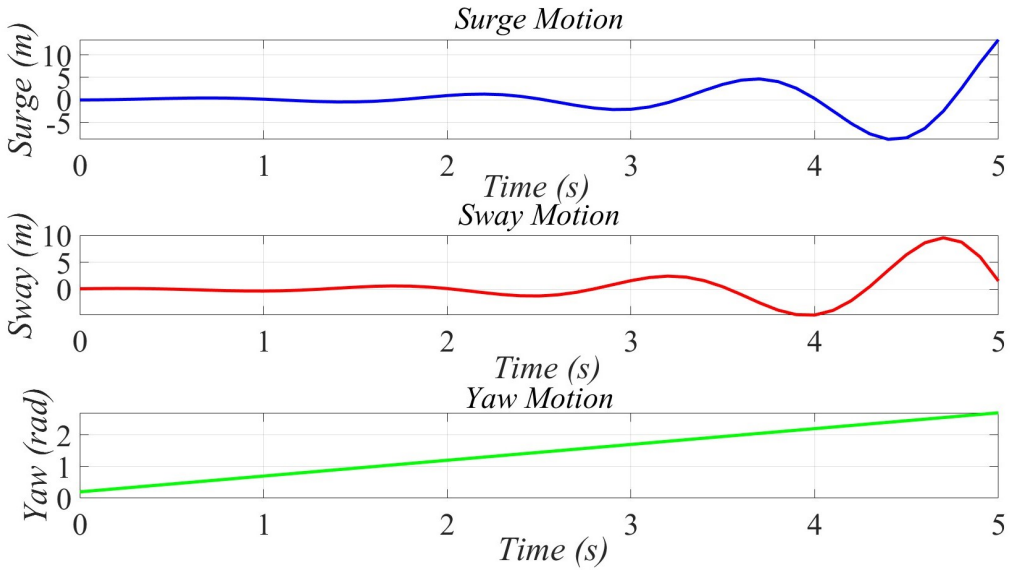


Figure 7. Wind effects represent water wave propagation with moored ship motion in rectangular domain.

3.5. Application of FVM on Paradip Port

Its construction aimed to assist the industries located in the states of Madhya Pradesh, Bihar, Uttar Pradesh, Jharkhand, Chhattisgarh, West Bengal, and Odisha. Depending on the situation, it may be lowered to any depth because of its soft underwater soil. A variety of goods can be handled by the entry channel, which is around 18 m deep. Inside the Paradip Port, six distinct locations (see Figure 8) were selected with ship sizes of 260,000 DWT (dead weight tonnage) to forecast the motion of moored ships (surge, sway, heave, roll, pitch, and yaw).



Figure 8. Six important sites (*S*01, *S*02, *S*03, *S*04, *S*05, *S*06) of a moored ship are shown in this figure of Paradip Port.

Six strategic ship positions inside Paradip Port were chosen in order to examine the translational and rotational motion characteristics of moored ships; see the Appendix A. These crucial spots, designated S01–S06, are displayed in Figure 8. In comparison to other places, ship positions *S*02, *S*03, and *S*05, *S*06 have a higher wave amplitude. The significant wave-induced oscillations at ship positions *S*02, *S*03, and *S*05 are most likely caused by the incident wave's numerous reflections off the port walls and corners. As a result, it may be said that, as the ship's position changes, the amplitude of its movements varies significantly.

Ship positions *S*01 and *S*05, *S*06 receive significant wave amplification in comparison to other ship locations, as seen by the pattern of amplification responses at various ship locations in Figure 9. Consequently, ship positions *S*01 and *S*05, *S*06 are chosen for in-depth examination of the motion reactions of the moored ships. The impact of energy dissipators on various ship movements is explained in the sections that follow. To lessen the motion of a moored ship for a certain approaching wave, several countermeasures are explored. For the motion of the moored ship, the frequency response function and wave exciting forces are calculated and examined.

If the incident wave's frequency coincides with the natural frequency of the harbor, it creates a strong amplification that is dangerous for the port's coastline structure and any moored ships. At strategic points inside the port, the resonance frequency (mode) is crucial for forecasting the incident wave field.

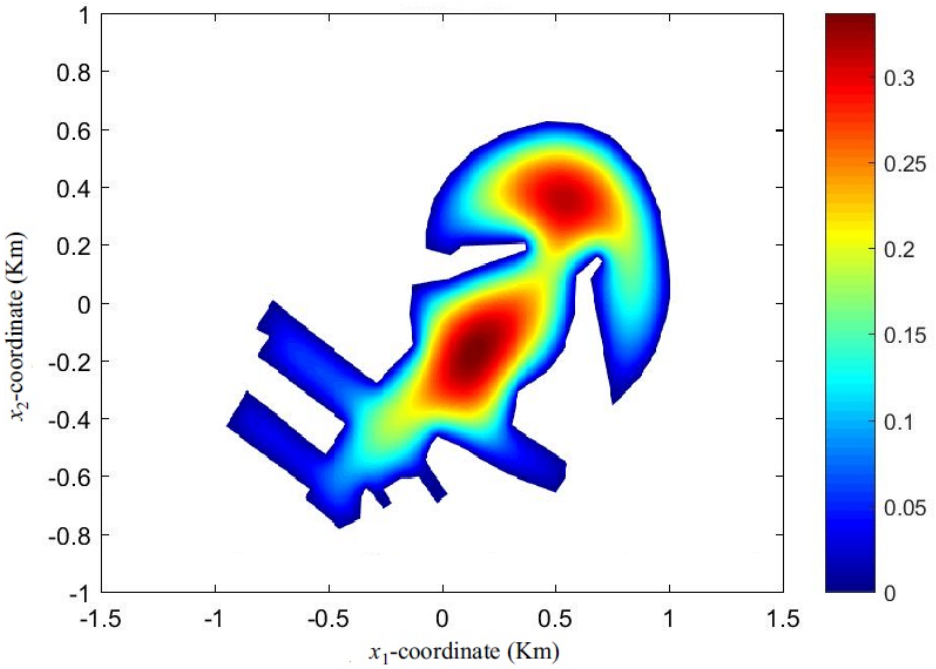


Figure 9. The true bathymetry of Paradip Port is provided, with depth variations ranging from 5 to 18 m in the port's interior region.

3.6. *Amplification Factor*

As seen in Figure 10, the amplification factor is assessed at sites S01 through S06 within Paradip Port, which are free of moored ships. The wave's amplification is calculated using a frequency interval of 0.01 and the normalized wave frequency (kL). The incoming wave is thought to have a wave angle of $\pi/3$ when it reaches the port opening. Wave numbers $k1 = 0.85$, $k2 = 1.8$, $k3 = 2.46$, $k4 = 2.63$, $k5 = 3.08$, $k6 = 3.86$, $k7 = 4.087$, and $k8 = 4.87$ are where the resonance modes are visible. The ship motion's wave amplitudes vary dramatically, with location changes for a particular frequency.

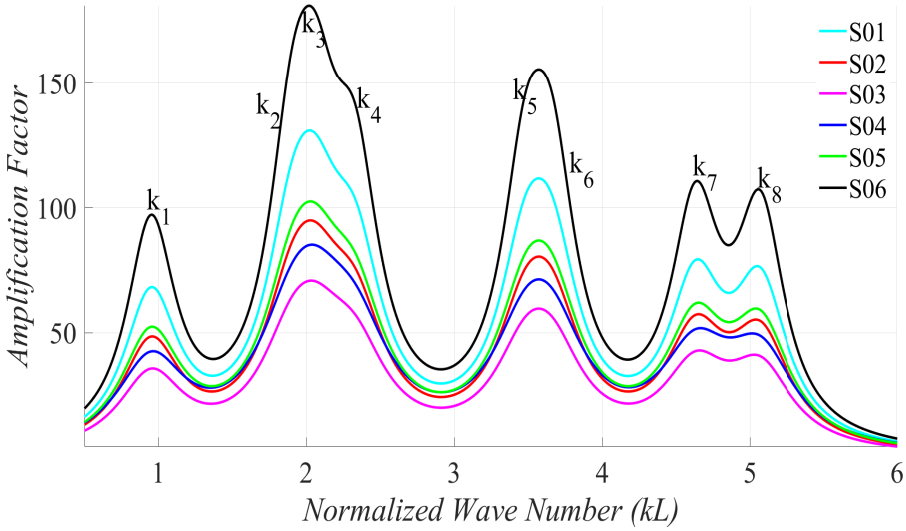


Figure 10. Paradip Port with key six locations (*S*01, *S*02, *S*03, *S*04, *S*05, *S*06) of a moored ship.

In comparison to other places, ship positions S02, S03, and S05, S06 have a higher wave amplitude. The many reflections of the incident wave with the port walls and corners are most likely the cause of the severe wave-induced oscillations at ship positions S02, S03, and S05. As a result, it may be said that, as the ship's position changes, the amplitude of its

movements varies significantly. Ship positions S01, S04, and S06 receive significant wave amplification in comparison to other ship locations, as seen by the pattern of amplification responses at various ship locations in Figure 10. Consequently, ship positions S01, S05, and S06 are chosen for in-depth examination of the motion reactions of the moored ships. The impact of energy dissipation on various ship movements is explained in the sections that follow. To lessen the motion of a moored ship for a certain approaching wave, several countermeasures are explored. For the motion of the moored ships, the frequency response function and wave exciting forces are calculated and examined.

3.7. Added Mass and Damping Coefficient

The motion of a moored ship within Paradip Port is examined using the present numerical approach. Ship movement is categorized into two types: translational and rotational. Translational motions include surge (movement along the x_1-axis), sway (movement along the x_2-axis), and heave (movement along the x_3-axis). Rotational motions consist of roll (rotation about the x_1-axis), pitch (rotation about the x_2-axis), and yaw (rotation about the x_3-axis), as depicted in Figure 11.

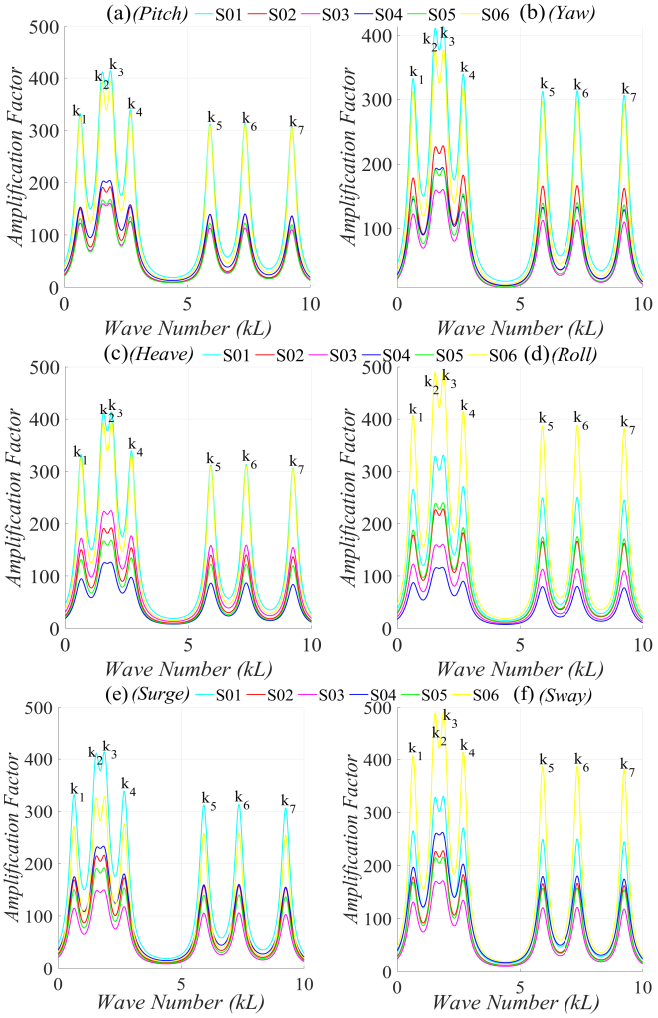


Figure 11. The amplification factor corresponding to the moored ship motions—including surge, sway, heave, roll, pitch, and yaw—is presented for locations *S*01, *S*02, *S*03, *S*04, *S*05, and *S*06. The wave numbers, k, indicate the points where the primary resonance peaks occur.

Figure 11 illustrates the amplification factor of the moored ship's motion within Paradip Port concerning the dimensionless wave number k_l, with an interval difference of $\Delta k = 0.01$ for six distinct locations: *S*01, *S*02, *S*03, *S*04, *S*05, and *S*06. The corresponding

dimensionless wave frequencies are specified as $k_1 = 0.64$, $k_2 = 1.52$, $k_3 = 1.90$, $k_4 = 2.69$, $k_5 = 5.91$, $k_6 = 7.35$, and $k_7 = 9.25$.

The resonance characteristics at six moored ship positions (S01, S02, S03, S04, S05, and S06) are analyzed under the influence of incident waves perpendicular to the harbor entrance. The amplitude response varies with location, with S04, S05, and S06 exhibiting greater values compared to the other positions. The high amplitude at S04 is primarily attributed to the direct exposure to incident waves, whereas at S05 and S06, it results from partial wave reflections at the port's sharp edges and internal walls. The key resonance modes for these locations, based on dimensionless wave frequencies, are found at $k_3 = 1.90, k_4 = 2.69, k_5 = 5.91, k_6 = 7.35$, and $k_7 = 9.25$. For translational motions, the dimensionless added mass is represented as $A_{ij}/M(i,j = 1,2,3)$, while for rotational motions, it is $A_{ij}/\omega M(i,j = 4,5,6)$. Similarly, the dimensionless damping coefficient is expressed as $B_{ij}/ML_s^2(i,j = 1,2,3)$ for translation and $B_{ij}/\omega ML_s^2(i,j = 4,5,6)$ for rotation, where M denotes the ship's mass and L_s represents its length. The x-axis is defined in terms of the non-dimensional frequency $\omega_2 L_s/g$. The hydrodynamic coefficients (added mass and damping) are investigated for varying water depth-to-draft ratios ($\delta = 1.2, \delta = 1.8, \delta = 2.4$) at location S06, with similar computations performed at S01 and S03. Additionally, ship motion for different incident wave angles ($\pi/4$, $\pi/2$, and $3\pi/4$) is examined for S01 and S03. Contributions to added mass coefficients are as follows: A_{11}/M (surge), A_{22}/M (sway), A_{33}/M (heave), A_{44}/ML_s^2 (roll), A_{55}/ML_s^2 (pitch), and A_{66}/ML_s^2 (yaw). The resonance peaks for surge-added mass (A_{11}/M) at an incident wave angle of $\pi/4$ occur at $f_1 = 0.063$, $f_2 = 0.066$, $f_3 = 0.310$, $f_4 = 0.311$, $f_5 = 0.388$, $f_6 = 0.475$, $f_7 = 0.476$, and $f_8 = 0.749$ (see Figure 12a–d). Similarly, the dominant peaks for sway-added mass (A_{22}/M) are at $f_1 = 0.063$, $f_2 = 0.069$, $f_3 = 0.310$, $f_4 = 0.311$, and $f_5 = 0.748$. The resonance locations for heave-added mass (A_{33}/M) are $f_1 = 0.064$, $f_2 = 0.069$, $f_3 = 0.310$, $f_4 = 0.311$, and $f_5 = 0.748$. For rotational motion, the resonance peaks in roll-added mass (A_{44}/ML_s^2) are found at $f_1 = 0.063$, $f_2 = 0.066$, $f_3 = 0.310$, $f_4 = 0.311$, $f_5 = 0.388$, $f_6 = 0.475$, $f_7 = 0.476$, and $f_8 = 0.748$. The peaks in pitch-added mass (A_{55}/ML_s^2) appear at $f_1 = 0.064$, $f_2 = 0.069$, $f_3 = 0.310$, $f_4 = 0.311$, and $f_5 = 0.749$. The yaw-added mass (A_{66}/ML_s^2) has peaks at $f_1 = 0.063$, $f_2 = 0.069$, $f_3 = 0.310$, $f_4 = 0.311$, and $f_5 = 0.748$. Global resonance peaks correspond to the dominant frequencies, while local resonance results from diffraction effects at breakwaters, harbor corners, and port boundaries. Consequently, port geometry significantly influences resonance characteristics. The analysis suggests that moored ships in Paradip Port exhibit stronger resonance effects in shallower waters, with resonance peaks diminishing as the water depth-to-draft ratio increases. The amplification factors at resonance frequencies are influenced by the water depth-to-draft ratio, making it a critical parameter in resonance studies. The major peaks in sway damping coefficient (B_{33}/ML_s^2) are identified in Figure 13a–d at $f_1 = 0.063$, $f_2 = 0.069$, $f_3 = 0.310$, $f_4 = 0.311$, and $f_5 = 0.748$. The resonance locations for heave damping coefficient (B_{44}/ML_s^2) are $f_1 = 0.064$, $f_2 = 0.069$, $f_3 = 0.310$, $f_4 = 0.311$, and $f_5 = 0.748$. For rotational damping, the roll damping coefficient (B_{55}/ML_s^2) has peaks at $f_1 = 0.063$, $f_2 = 0.066$, $f_3 = 0.310$, $f_4 = 0.311$, $f_5 = 0.388$, $f_6 = 0.475$, $f_7 = 0.476$, and $f_8 = 0.748$. These results emphasize the importance of port design and water depth in moored ship dynamics.

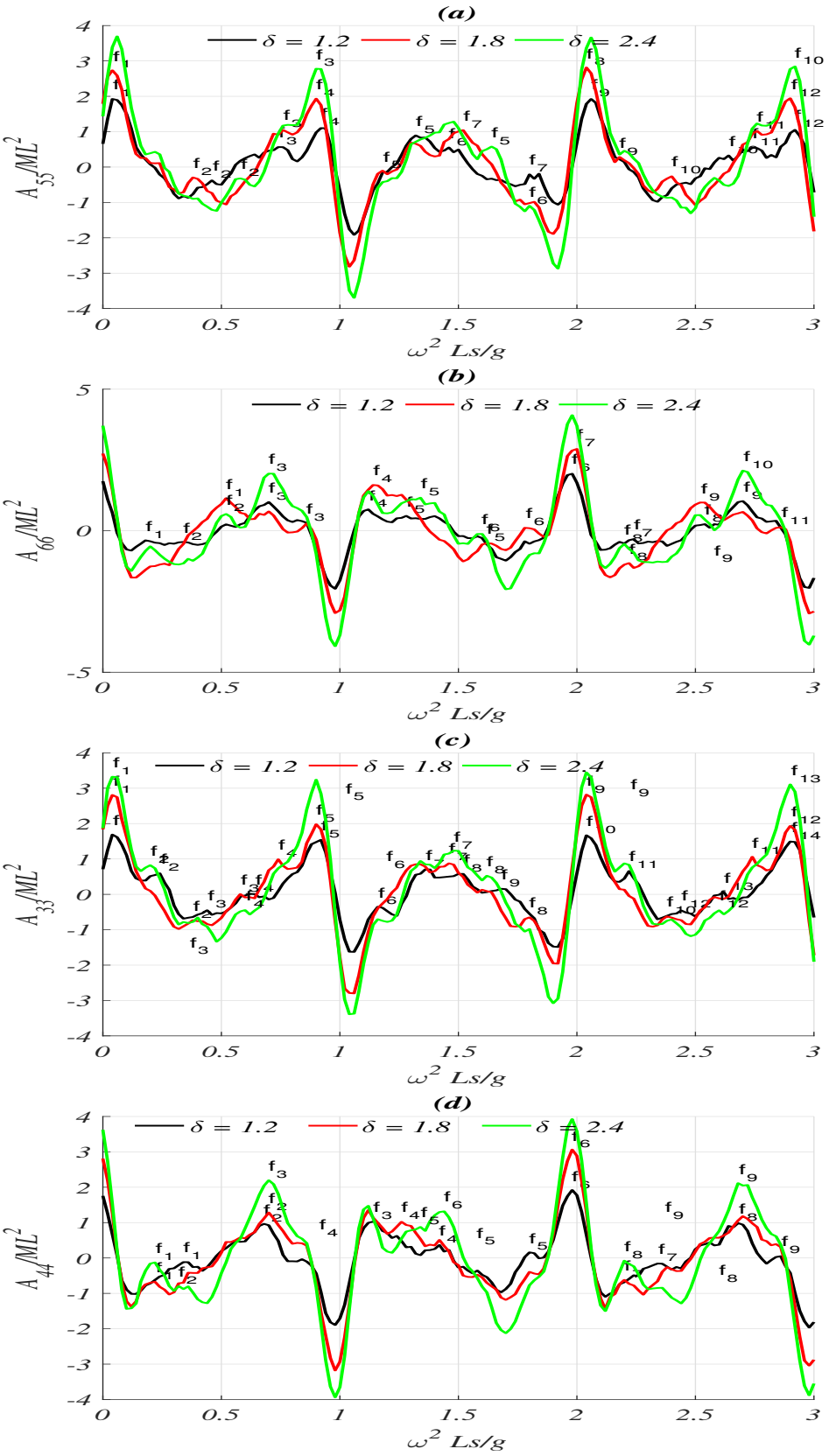


Figure 12. The angle of incident waves is taken into account for the record station S06 as $\beta = \pi/4$. For the various values of $\delta = 1.2, \delta = 1.8$, and $\delta = 2.4$, with the sampling interval frequency $\Delta f = 0.002$, the surge-added mass (A33/M), the sway-added mass (A44/M), the heave-added mass (A55/M), the roll-added mass (B66/MLs2).

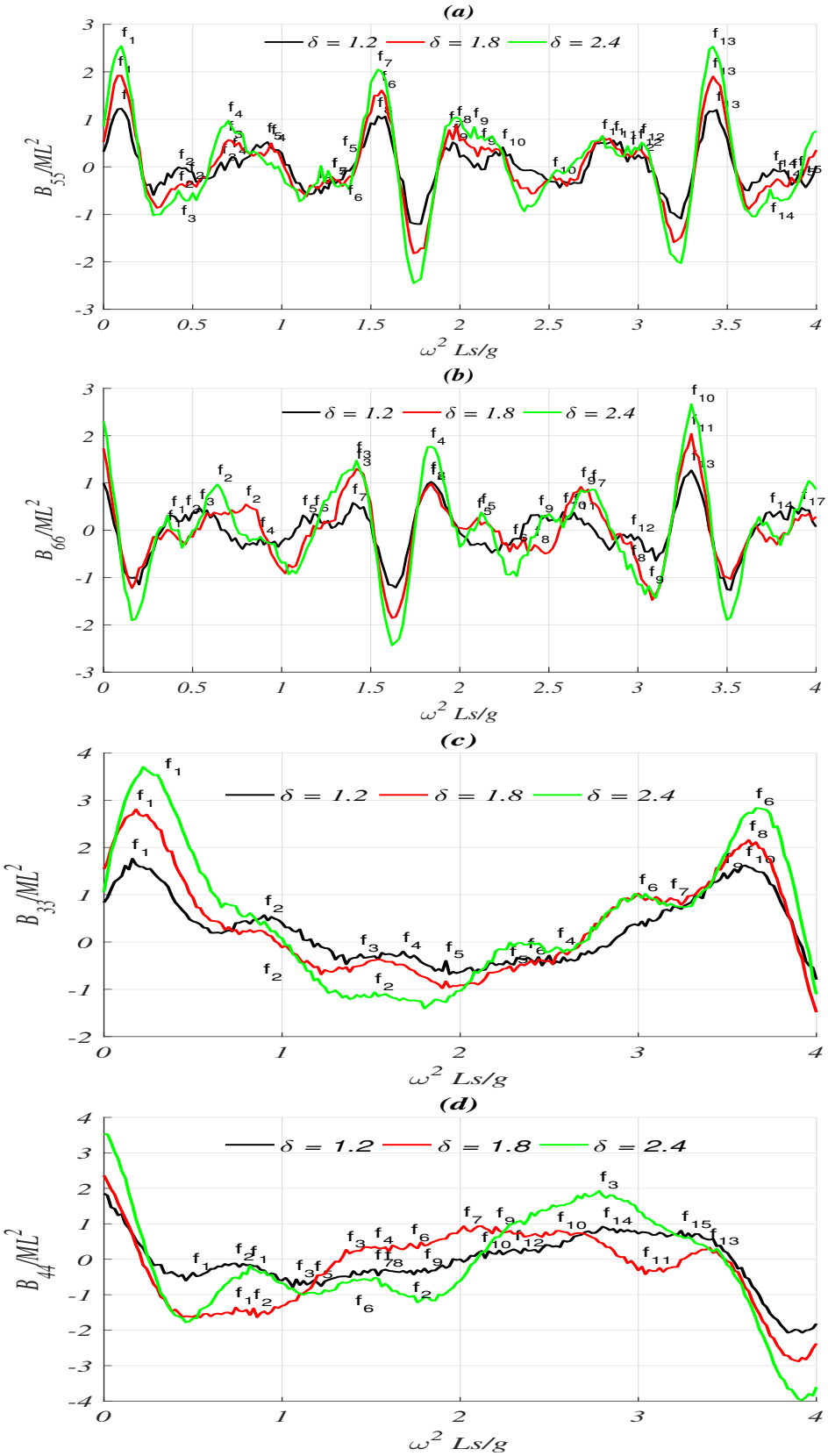


Figure 13. The angle of incident waves is taken into account for the record station S06 as $\beta = \pi/4$. For the various values of $\delta = 1.2, \delta = 1.8$, and $\delta = 2.4$, with the sampling interval frequency f, the surge damping (B33/M), the sway-added damping (B44/M), the heave damping (B55/M), the roll-added damping (B66/MLs2).

The pitch-damping coefficient (B_{66}) exhibits peak values for an incident wave angle of $\pi/4$ at frequencies $f_1 = 0.064$, $f_2 = 0.069$, $f_3 = 0.310$, $f_4 = 0.311$, and $f_5 = 0.749$. Similarly, the resonance peaks corresponding to the yaw-damping coefficient ($B_{66}/\omega MLs^2$) occur at $f_1 = 0.063$, $f_2 = 0.069$, $f_3 = 0.310$, $f_4 = 0.311$, and $f_5 = 0.748$. For translational motions including surge, sway, and heave, the first four resonance peaks remain consistent, while variations in subsequent peaks are attributed to local resonance effects within the port and harbor. Additionally, the resonance peaks for rotational damping coefficients—specifically roll, pitch, and yaw—align well with their respective added mass values. This correlation indicates that the wave incidence direction and the depth-to-draft ratio significantly influence the hydrodynamic damping characteristics.

3.8. Evolution of Wave Oscillations

To assess the sea surface wave dynamics within the port, numerical simulations were carried out using real bathymetric and topographic data of Paradip Port. These simulations modeled the interaction of incoming ocean waves with the port's internal structures, particularly when waves approached perpendicularly to the entrance. Due to the presence of multiple sharp corners along the port boundary, finer grid discretization was applied near these corner regions to ensure accuracy in capturing wave reflections and diffraction.

To measure the wave field close to the moored ship area, six ships were positioned inside Paradip Port. The sea surface wave field is displayed in Figure 14 at the first four resonance modes (k1 = 0.62, k2 = 0.84, k3 = 1.23, and k4 = 1.62).

The wave elevations at moored ship locations *S*02, *S*03, *S*04, *S*05, and *S*06 exhibit significant amplification at the primary resonance mode, as depicted in Figure 14a, with the exception of site *S*01. At ship positions *S*05 and *S*06, the intense oscillations induced by incident waves at resonance $k_2 = 0.84$ (see Figure 14b) present challenges for loading and unloading operations.

When the incident wave propagates with resonance mode $k_3 = 1.23$ (Figure 14c), strong oscillations are observed around ship sites *S*02, *S*03, *S*05, and *S*06, in contrast to other ship locations. Similarly, Figure 14d illustrates that the incident wave at resonance mode $k_4 = 1.63$ generates intense oscillations near site *S*06 compared to other locations.

Given these resonance effects, ship sites *S*01 and *S*04 remain relatively stable for moored ship loading and unloading under these specific wave conditions. Additionally, locations *S*02, *S*03, *S*04, and *S*05 offer moderate safety for loading and unloading during this event. A minor resonance effect is also observed along the back wall near *S*02 and *S*03, whereas a stronger resonance occurs on the opposite side of the berthing area at Paradip Port.

Overall, compared to other resonance modes, the fourth resonance mode's wave amplitude intensity (k4 = 1.62) is the greatest. The wave amplitude at the berthing position decreased in both the first and second resonance modes. Consequently, loading and unloading may be carried out during incident waves with first and second resonance since the wave amplitude is lower than that of the higher resonance modes. All things considered, S01, S02, S03, and S04 are the safe spots for moored ships for the various resonance modes.

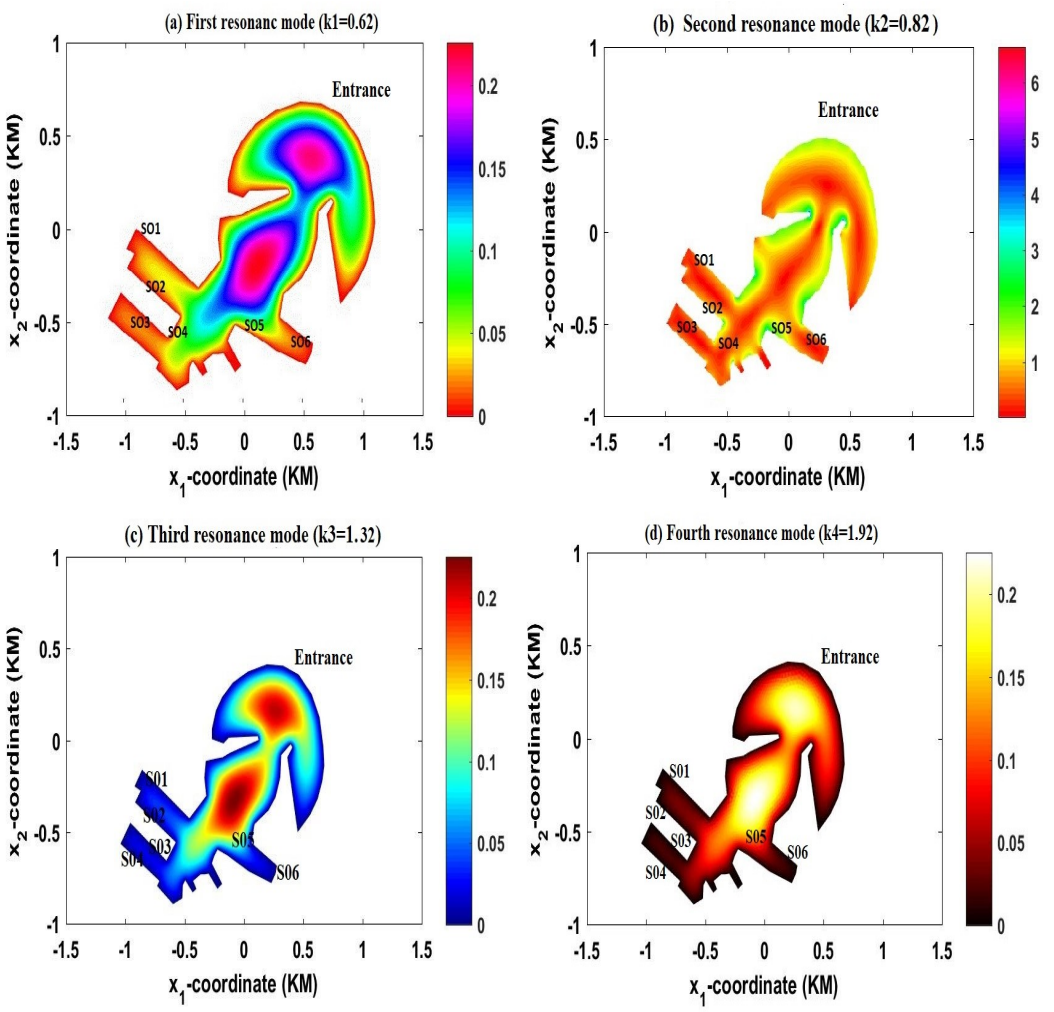


Figure 14. Four distinct resonance modes are observed in the sea surface wave field within Paradip Port: (**a**) the primary resonance mode at $k_1 = 0.62$, (**b**) the second resonance mode at $k_2 = 0.82$, (**c**) the third resonance mode at $k_3 = 1.32$, and (**d**) the fourth resonance mode at $k_4 = 1.92$. The moored vessel within the port experiences these resonance effects, which influence its motion and stability.

Figure 15 shows the surge displacement of the ship over time. Initially, the displacement oscillates with a small amplitude, but over time, the amplitude increases as the ship interacts with the incoming waves. This is typical for a moored ship subjected to wave forces as the wave energy builds up and the system reaches a state of resonant oscillation. The damping present in the system limits the growth of the amplitude, but the oscillations still gradually increase in magnitude until they stabilize. Figure 15 shows the effect of the wave spectral parameter β on the surge displacement. As β increases, the wave spectrum shifts towards higher frequencies, increasing the energy at higher frequencies. This results in a more pronounced effect on the ship's surge motion, causing larger oscillations over time. Conversely, smaller values of β correspond to a more uniform wave spectrum, which leads to less intense oscillations and a smaller overall response. From the simulation results, it is evident that β plays a critical role in determining the intensity of the ship's motion. By adjusting β, the response of the ship can be tailored to specific conditions, which is crucial for designing effective mooring systems and ensuring the stability of ships in varying sea states.

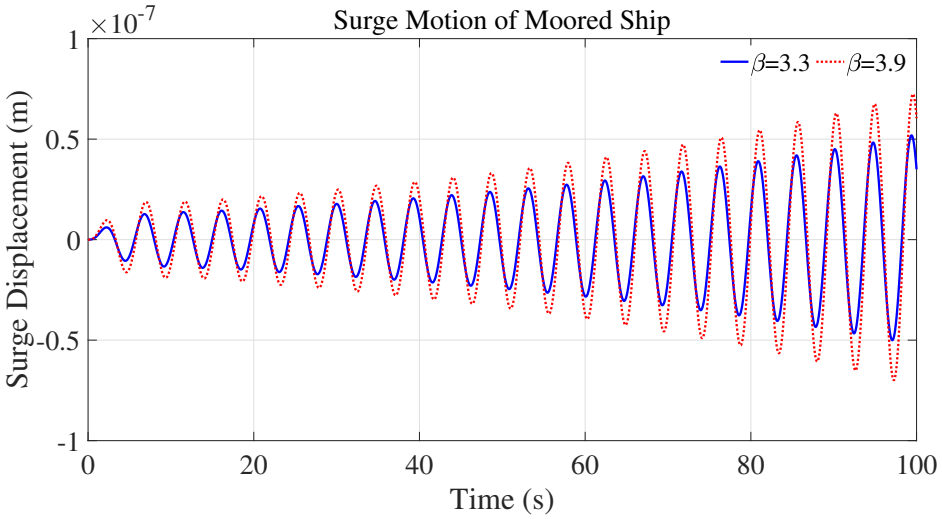


Figure 15. Surged displacement motions for different wave spectral parameters: $\beta = 3.3, 3.9$.

4. Discussion and Conclusions

The motion of moored ships at Paradip Port in Odisha, India, at important locations *S*01, *S*02, *S*03, *S*04, *S*05, and *S*06 under various incident wave angles is analyzed numerically in this study. The numerical model's main goal is to locate safe areas for moored ships in Paradip Port when resonance conditions exist. The findings indicate that wave oscillations decrease as the depth–draft ratio (δ) increases, highlighting that anchored ships in shallow waters experience more pronounced wave amplification compared to those in deeper regions. Furthermore, for various water depths, the precise amplification of each moored ship motion mode is determined.

Beyond these findings, this study has broader implications for port and harbor design, mooring safety, and ship stability under resonant conditions. The numerical framework presented here can be extended to analyze different port configurations with varying seabed topographies and alternative mooring arrangements to enhance ship stability. Additionally, the approach can be applied to other marine structures, such as floating platforms and offshore wind turbines, which are also subject to nonlinear wave forces. Further, investigating different wave conditions, including extreme weather scenarios and multi-directional wave interactions, would provide a more comprehensive understanding of port resonance mitigation. Moreover, integrating environmental forces such as wind and tidal currents into the numerical model could enhance predictive capabilities and support more resilient harbor designs.

It is proposed that the nonlinear response of a moored structure in confined waters can be effectively predicted by integrating linear potential theory for wave-body interactions with a modified Boussinesq model for nonlinear wave propagation over a gradually sloping bathymetry. This hybrid approach ensures a more accurate representation of wave dynamics in coastal and harbor environments. To establish the reliability and accuracy of the numerical framework, a convergence analysis is performed. The study examines moored ship motion at six distinct locations within Paradip Port, identifying six primary motion modes: surge, sway, heave, pitch, roll, and yaw. The key resonance peaks occur at wave frequencies $k = 1.90, k = 2.69, k = 5.92, k = 7.35$, and $k = 9.25$, highlighting the critical conditions that influence moored ship behavior.

Simulation results indicate that the most vulnerable locations within Paradip Port for loading and unloading operations are moored ship sites S04, S05, and S06. These locations exhibit significant ship motion responses under specific wave conditions, emphasizing the necessity for optimized mooring strategies to enhance operational safety. Additionally,

at ship location S06, the study explores variations in the damping coefficient and added mass under incident wave angles of $\frac{\pi}{4}$ and $\frac{\pi}{2}$, considering different values of δ, which represents the ratio of the ship draft to the sea depth. Beyond numerical validation, this study provides a comprehensive framework for evaluating moored ship dynamics in complex harbor environments. The findings contribute to improved maritime safety-optimized port operations and enhanced design strategies for mooring systems. Future research can further refine this model by incorporating additional hydrodynamic influences, real-time environmental variations, and advanced computational techniques for greater predictive accuracy.

Author Contributions: Vinita, conceptualization, methodology, numerical modeling, formal analysis, and investigation, writing—original draft preparation, validation, and verification; P.K., conceptualization, writing—review and editing, supervision. All authors have read and agreed to the published version of the manuscript.

Funding: This research is not supported by any funding agency.

Institutional Review Board Statement: Not applicable.

Informed Consent Statement: Not applicable.

Data Availability Statement: Numerical simulation data can be made available on request.

Acknowledgments: The authors would like to acknowledge the Department of Applied Sciences, National Institute of Technology, Delhi, for their sincere support.

Conflicts of Interest: The authors declare that they do not possess any identifiable conflicting financial interests or personal relationships that may have potentially influenced the findings presented in this research article.

Appendix A

To accurately model the hydrodynamic interactions of moored ships, it is essential to define their geometric and physical properties. Table A1 provides detailed specifications, including ship dimensions, weight, center of gravity (CG), and center of buoyancy (CB).

Table A1. Specifications of moored ships.

Ship	Length (m)	Beam (m)	Draft (m)	Weight (tons)	CG (m)	CB (m)
Ship 1	150	25	8	12,000	(75, 12, 5)	(74, 12, 4)
Ship 2	200	30	10	18,000	(100, 15, 6)	(99, 15, 5)
Ship 3	180	28	9	16,000	(90, 14, 5.5)	(89, 14, 4.8)

The information in Table A1 is crucial for analyzing the dynamic behavior of moored ships under external forces such as waves, currents, and winds. The length, beam, and draft significantly influence the hydrodynamic response of a vessel. Longer ships generally have lower wave-induced motions, while beam and draft determine stability and wave resistance. The displacement weight affects how the ship interacts with the water. Heavier ships have greater inertia, impacting their response to wave forces. The center of buoyancy (CB) represents the centroid of the displaced water volume, which plays a crucial role in stability calculations. The center of gravity (CG) determines the ship's balance. If CG is too high, the vessel may experience excessive rolling. The relative positions of CG and CB influence the metacentric height, a key factor in stability assessments.

References

1. Havelock, T.H. The propagation of groups of waves in dispersive media with application to waves on water produced by a travelling disturbance. *Proc. R. Soc. Lond. Ser. Contain. Pap. Math. Phys. Character* **1908**, *81*, 398–430.
2. Johnson, J. Ship waves in navigation channels. *Coast. Eng. Proc.* **1957**, *1*, 40. [CrossRef]
3. Kravtchenko, J.; McNown, J.S. Seiche in rectangular ports. *Q. Appl. Math.* **1955**, *13*, 19–26. [CrossRef]
4. Ippen, A.T.; Goda, Y. *Wave Induced Oscillations in Harbors: The Solution for a Rectangular Harbor Connected to the Open-Sea*; Massachusetts Institute of Technology: Cambridge, MA, USA, 1963.
5. Lee, J.J. *Wave Induced Oscillations in Harbors of Arbitrary Shape*; Report No. KH-R-20; W.M. Keck Laboratory of Hydraulics and Water Resources: La Jolla, CA, USA, 1969.
6. Chou, C.R.; Lin, J.G. BEM analysis of oscillation in harbor of arbitrary shaped with uneven sea bed. In Proceedings of the 8th International Conference on Ocean Engineering, Ho Chi Minh, Vietnam, 27–29 November 202; pp. 111–130.
7. Chou, C.-R.; Han, W.-Y. Wave-induced oscillations in harbours with dissipating quays. *Coast. Eng. Jpn.* **1993**, *36*, 1–23. [CrossRef]
8. Kumar, P. Gulshan. Extreme wave-induced oscillation in Paradip Port under the resonance conditions. *Pure Appl. Geophys.* **2017**, *174*, 4501–4516. [CrossRef]
9. Chou, C.R.; Han, W.Y. Oscillations induced by irregular waves in harbours. In Proceedings of the 24th International Conference on Coastal Engineering ASCE, Kobe, Japan, 23–28 October 1994; pp. 2987–3001.
10. Kumar, P. Theoretical analysis of extreme wave oscillation in Paradip Port using a 3D boundary element method. *Ocean. Eng.* **2018**, *164*, 13–22. [CrossRef]
11. Kumar, P. Modeling of shallow water waves with variable bathymetry in an irregular domain by using hybrid finite element method. *Comput. Fluids* **2018**, *165*, 386–398. [CrossRef]
12. Bellotti, G. Transient response of harbours to long waves under resonance conditions. *Coast. Eng.* **2007**, *54*, 680–693. [CrossRef]
13. Gao, J.; Ji, C.; Gaidai, O.; Liu, Y.; Ma, X. Numerical investigation of transient harbor oscillations induced by N-waves. *Coast. Eng.* **2017**, *125*, 119–131. [CrossRef]
14. Gao, J. Numerical study on transient harbor oscillations induced by successive solitary waves. *Ocean Dyn.* **2018**, *68*, 193–209. [CrossRef]
15. Gao, J.; Zhou, X.; Zang, J.; Chen, Q.; Zhou, L. Influence of offshore fringing reefs on infragravity period oscillations within a harbor. *Ocean Eng.* **2018**, *158*, 286–298. [CrossRef]
16. Gao, J.; Zhou, X.; Zhou, L.; Zang, J.; Chen, H. Numerical investigation on effects of fringing reefs on low-frequency oscillations within a harbor. *Ocean Eng.* **2019**, *172*, 86–95. [CrossRef]
17. Kumar, P.; Zhang, H.; Yuen, D.A.; Kim, K.I. Wave field analysis in a harbor with irregular geometry through boundary integral of Helmholtz equation with corner contributions. *Comput. Fluids* **2013**, *88*, 287–297. [CrossRef]
18. Kumar, P.; Zhang, H.; Kim, K.I.; Shi, Y.; Yuen, D.A. Wave spectral modeling of multidirectional random waves in a harbor through combination of boundary integral of Helmholtz equation with Chebyshev point discretization. *Comput. Fluids* **2015**, *108*, 13–24. [CrossRef]
19. Kwak, M.; Pyun, C. Numerical analysis of moored ship motion considering harbor resonance in Pohang New Harbor. In Proceedings of the 7th International Conference of Asian and Pacific Coasts (APAC 2013), Bali, Indonesia, 24–26 September 2013; pp. 750–757.
20. Guerrini, M.; Bellotti, G.; Fan, Y.; Franco, L. Numerical modelling of long waves amplification at Marina di Carrara Harbour. *Appl. Ocean Res.* **2014**, *48*, 322–330. [CrossRef]
21. Lopez, M.; Iglesias, G.; Kobayashi, N. Long period oscillations and tidal level in the Port of Ferrol. *Appl. Ocean Res.* **2012**, *38*, 126–134. [CrossRef]
22. Gao, J.; Hou, L.; Liu, Y.; Shi, H. Influences of bragg reflection on harbor resonance triggered by irregular wave groups. *Ocean. Eng.* **2024**, *305*, 117941. [CrossRef]
23. Gao, J.; Ma, X.; Dong, G.; Chen, H.; Liu, Q.; Zang, J. Investigation on the effects of Bragg reflection on harbor oscillations. *Coast. Eng.* **2021**, *170*, 103977. [CrossRef]
24. Gao, J.; Shi, H.; Zang, J.; Liu, Y. Mechanism analysis on the mitigation of harbor resonance by periodic undulating topography. *Ocean. Eng.* **2023**, *281*, 114923. [CrossRef]
25. Gonzalez-Marco, D.; Sierra, J.P.; De Ybarra, F.O.; Sánchez-Arcilla, A. Implications of long waves in harbor management: The Gijón port case study. *Ocean Coast. Manag.* **2018**, *51*, 180–201. [CrossRef]
26. Kofoed-hansen, H.; Kerper, D.R.; Sørensen, O.R.; Kirkegaard, J. Simulation of long wave agitation in ports and harbours using a time-domain boussinesq model. In Proceedings of the Fifth International Symposium on Ocean Wave Measurement and Analysis—Waves 2005, Madrid, Spain, 3–7 July 2005; pp. 1–11.

27. Ohyama, T.; Tsuchida, M. Expanded mild-slope equations for the analysis of wave-induced ship motion in a harbor. *Coast. Eng.* **1997**, *30*, 77–103. [CrossRef]
28. Lee, H.S.; Kim, S.D.; Wang, K.H.; Eom, S. Boundary element modeling of multidirectional random waves in a harbor with a rectangular navigation channel. *Ocean Eng.* **2009**, *36*, 1287–1294. [CrossRef]
29. Sharma, A.; Panchang, V.G.; Kaihatu, J.M. Modeling nonlinear wave-wave interactions with the elliptic mild slope equation. *Appl. Ocean Res.* **2014**, *48*, 114–125. [CrossRef]
30. Cerrato, A.; Rodríguez-Tembleque, L.; González, J.A.; Aliabadi, M.F. A coupled finite and boundary spectral element method for linear water-wave propagation problems. *Appl. Math. Model.* **2017**, *48*, 1–20. [CrossRef]
31. Servan-Camas, B.; Gutierrez-Romero, J.E.; Garcia-Espinosa, J. A time-domain second-order FEM model for the wave diffraction-radiation problem. Validation with a semisubmersible platform. *Mar. Struct.* **2018**, *58*, 278–300. [CrossRef]
32. Chen, C.; Liu, H.; Beardsley, R. An unstructured grid, finite volume, three-dimensional, primitive equations ocean model: Application to coastal ocean and estuaries. *J. Atmos. Ocean Technol.* **2003**, *20*, 159–186. [CrossRef]
33. Dusseljee, D.; Klopman, G.; van Vledder, G.; Riezebos, H. Impact of harbor navigation channels on waves: A numerical modelling guideline. *Coast. Eng. Proc.* **2014**, *1*, 58. [CrossRef]
34. Sawaragi, T.; Aoki, S.; Hamamoto, S. Analysis of hydrodynamic forces due to waves acting on a ship in a harbour of arbitrary geometry. In Proceedings of the 8th International Conference on Offshore Mechanics and Arctic Engineering, The Hague, The Netherlands, 19–23 March 1989; pp. 117–123.
35. Kwak, M.; Moon, Y.; Pyun, C. Computer simulation of moored ship motion induced by harbor resonance in Pohang New Harbor. *Coast. Eng. Proc.* **2012**, *1*, 68. [CrossRef]
36. Ohyama, T.; Tsuchida, M. Development of a partially three dimensional model for ship motion in a harbor with arbitrary bathymetry. *Coast. Eng.* **1995**, *1994*, 871–885.
37. Takagi, K.; Naito, S.; Hirota, K. Hydrodynamic forces acting on a floating body in a harbor of arbitrary geometry. In Proceedings of the 3rd International Conference Offshore and Polar Engineering, Singapore, 6–11 June 1993; Volume 4, pp. 97–104.
38. Yoo, B.S. *An Analysis of Ship Motion in a Harbor*; Seoul National University: Seoul, Republic of Korea, 1998; Volume 192.
39. Madsen, P.A.; Sorensen, O.R. A new form of Boussinesq equations with improved dispersion characteristics. Part 2 A slowlyvarying bathymetry. *Coast. Eng.* **1992**, *18*, 183–204. [CrossRef]
40. Bingham, H.B. A hybrid Boussinesq-panel method for predicting the motion of a moored ship. *Coast. Eng.* **2000**, *40*, 21–38. [CrossRef]
41. Sakakibara, S.; Takeda, S.; Iwamoto, Y.; Kubo, M. A hybrid potential theory for predicting the motions of a moored ship induced by large-scaled tsunami. *Ocean Eng.* **2010**, *37*, 1564–1575. [CrossRef]
42. Kim, B.W.; Sung, H.G.; Kim, J.H.; Hong, S.Y. Comparison of linear spring and nonlinear FEM methods in dynamic coupled analysis of floating structure and mooring system. *J. Fluids Struct.* **2013**, *42*, 205–227. [CrossRef]
43. Bhautoo, P.; Mortensen, S.; Hibberd, W.; Harkin, A.; Kirkegaard, J.; Morley, B. Moored vessel interaction induced by passing ships at the Port of Brisbane. In Proceedings of the Australasian Coasts & Ports Conference 2015, 22nd Australasian Coastal and Ocean Engineering Conference and the 15th Australasian Port and Harbour, Conference, Auckland, New Zealand, 15–18 September 2015; pp. 75–82.
44. Figuero, A.; Sande, J.; Peña, E.; Alvarellos, A.; Rabuñal, J.R.; Maciñeira, E. Operational thresholds of moored ships at the oil terminal of inner port of A Coruña (Spain). *Ocean Eng.* **2019**, *172*, 599–613. [CrossRef]
45. Watai, R.D.A.; Ruggeri, F.; Tannuri, E.A.; Santos, N.F.; Tavares, B.R.; dos Santos, J.M.G. An analysis methodology for the passing ship problem considering real-time simulations and moored ship dynamics: Application to the Port of Santos, in Brazil. *Appl. Ocean Res.* **2018**, *80*, 148–165. [CrossRef]
46. Bayraktar, D.; Beji, S. Numerical simulation of waves generated by a moving pressure field. *Ocean Eng.* **2013**, *59*, 231–239. [CrossRef]
47. Fraccarollo, L.; Toro, E.F. Experimental and numerical assessment of the shallow water model for two-dimensional dam-break type problems. *J. Hydraul. Res.* **1995**, *33*, 843–864. [CrossRef]
48. Kim, Y.; Kim, K.H.; Kim, J.H. Time-domain analysis of nonlinear motion responses and structural loads on ships and offshore structures : Development of WISH programs. *Int. J. Nav. Archit. Ocean Eng.* **2011**, *3*, 37–52. [CrossRef]
49. Kumar, P.; Zhang, H.; Ik, K.; Yuen, D.A. Modeling wave and spectral characteristics of moored ship motion in Pohang New Harbor under the resonance conditions. *Ocean Eng.* **2016**, *119*, 101–113. [CrossRef]
50. Pessoa, J.; Fonseca, N.; Soares, C.G. Numerical study of the coupled motion responses in waves of side-by-side LNG floating systems. *Appl. Ocean Res.* **2015**, *51*, 350–366. [CrossRef]

51. Antuono, M.; Liapidevskii, V.; Brocchini, M. Dispersive nonlinear shallow-water equations. *Stud. Appl. Math.* **2009**, *122*, 1–28. [CrossRef]
52. Kim, S.; Lee, S.; Kim, K.H. Wavenumber-extended high-order oscillation control finite volume schemes for multi-dimensional aeroacoustic computations. *J. Comput. Phys.* **2008**, *227*, 4089–4122. [CrossRef]

Disclaimer/Publisher's Note: The statements, opinions and data contained in all publications are solely those of the individual author(s) and contributor(s) and not of MDPI and/or the editor(s). MDPI and/or the editor(s) disclaim responsibility for any injury to people or property resulting from any ideas, methods, instructions or products referred to in the content.